Mon. Not. R. Astron. Soc. **000**, 000–000 (0000) Printed 2 February 2009 (MN LaTeX style file v2.2)

Post-starburst galaxies: more than just an interesting curiosity

Vivienne Wild[1,2⋆], C. Jakob Walcher[2], Peter H. Johansson[3], Laurence Tresse[4],
Stéphane Charlot[2], Agnieszka Pollo[5], Olivier Le Fèvre[4], Loic de Ravel[4]
[1] *Max-Planck Institut für Astrophysik, Karl-Schwarzschild Str. 1, 85741 Garching, Germany*
[2] *Institut d'Astrophysique de Paris, UMR 7095, 98 bis Bvd Arago, 75014 Paris, France*
[3] *Universitäts-Sternwarte München, Scheinerstr. 1, D-81679 München, Germany*
[4] *Laboratoire d'Astrophysique de Marseille (UMR 6110), CNRS-Université de Provence, BP 8, 13376 Marseille Cedex 12, France*
[5] *The Andrzej Soltan Institute for Nuclear Studies, ul. Hoza 69, 00-681 Warszawa, Poland*

2 February 2009

arXiv:0810.5122v2 [astro-ph] 2 Feb 2009

ABSTRACT

From the VIMOS VLT DEEP Survey (VVDS) we select a sample of 16 galaxies with spectra which identify them as having recently undergone a strong starburst and subsequent fast quenching of star formation. These post-starburst galaxies lie in the redshift range $0.5 < z < 1.0$ with masses $> 10^{9.75} M_{\odot}$. They have a number density of 1×10^{-4} per Mpc^3, almost two orders of magnitude sparser than the full galaxy population with the same mass limit. We compare with simulations to show that the galaxies are consistent with being the descendants of gas rich major mergers. Starburst mass fractions must be larger than $\sim 5 - 10\%$ and decay times shorter than $\sim 10^8$ years for post-starburst spectral signatures to be observed in the simulations. We find that the presence of black hole feedback does not greatly affect the evolution of the simulated merger remnants through the post-starburst phase. The multiwavelength spectral energy distributions (SEDs) of the post-starburst galaxies show that 5/16 have completely ceased the formation of new stars. These 5 galaxies correspond to a mass flux entering the red-sequence of $\dot{\rho}_{A\rightarrow Q,PSB} = 0.0038^{+0.0004}_{-0.001}$ M$_{\odot}$/Mpc^3/yr, assuming the defining spectroscopic features are detectable for 0.35 Gyr. If the galaxies subsequently remain on the red sequence, this accounts for 38^{+4}_{-11}% of the growth rate of the red sequence. Finally, we compare our high redshift results with a sample of galaxies with $0.05 < z < 0.1$ observed in the Sloan Digital Sky Survey (SDSS) and UKIRT Infrared Deep Survey (UKIDSS). We find a very strong redshift evolution: the mass density of strong post-starburst galaxies is 230 times lower at $z \sim 0.07$ than at $z \sim 0.7$.

Key words: galaxies: high redshift, evolution, stellar content, mass function; methods: statistical

1 INTRODUCTION

Since Hubble (1926), the bimodality in the distribution of galaxy properties has been one of the great curiosities in the field of astronomy. Bimodality is observed in galaxy colours, morphology, star formation rates and galaxy stellar masses. Modern spectroscopic galaxy surveys have allowed us to quantify the bimodality precisely, especially with the advent of the Sloan Digital Sky Survey (SDSS) (Strateva et al. 2001; Kauffmann et al. 2003b; Baldry et al. 2004). Even at high redshift, evidence for bimodality in the galaxy population is being sought and found (Bundy et al. 2005; Willmer et al. 2006; Franzetti et al. 2007).

Recent observations have revealed that since a redshift of around unity the total mass of stars living in red sequence galaxies has increased by a factor of two (Bell et al. 2004). At the same time, the stellar mass density of the blue sequence has remained almost constant. The interpretation is that some blue galaxies migrate onto the red sequence after the quenching of their star formation, whilst the remainder continue to form new stars (e.g. Faber et al. 2007; Arnouts et al. 2007). This quenching of star formation is apparently occurring in galaxies of increasingly lower masses as the Universe ages (Bundy et al. 2006). So-called "dry" (gas poor) mergers, with little associated star formation, can increase individual galaxy masses within the red-sequence, forming the massive ellipticals seen today (van Dokkum 2005; Bell et al. 2006). As well as allowing the building of very massive ellipticals, such a scenario matches the observed kinematic and photometric properties of present-day ellipticals (Naab et al. 2006, 2007).

The overall decrease in global SFR density since $z \sim 1$ appears to be caused by a gradual decline in the mean SFR of galaxies,

---

⋆ wild@iap.fr

rather than a decrease in the number of starbursts (Hammer et al. 1997; Noeske et al. 2007; Tresse et al. 2007). However, the process, or processes, responsible for this gradual decline remain to be determined. What physical mechanisms cause a galaxy to stop forming stars, to turn into a spheroid, and thus to enter the red sequence? There are many competing theories which address one or both of these problems. Hot gas stripping (sometimes called strangulation) of small galaxies as they fall into overdense environments leads to a slow quenching of their star formation (Larson et al. 1980; Balogh & Morris 2000; van den Bosch et al. 2008). In regions of high external pressure, the cold gas may also be stripped from the galaxies by ram pressure stripping (Gunn & Gott 1972; Cayatte et al. 1994). Gas rich major mergers may perform both tasks, causing a starburst that is strong enough to rapidly exhaust the supply of fuel, and convert the disk galaxies into spheroids (Toomre & Toomre 1972; Barnes & Hernquist 1992; Naab & Burkert 2003). In this latter scenario, subsequent cooling from the inter-galactic medium may cause a disk to reform and return the galaxy to the blue sequence. Therefore, the existence and efficient coupling to the ISM of additional mechanical energy from a central active nucleus (often called AGN feedback) has been proposed to prevent refueling and allow the red sequence to build (Springel et al. 2005a; Hopkins et al. 2007; Khalatyan et al. 2008). Observational evidence for the existence, but above all the relative importance of each of these scenarios, remains scarce.

Much progress has been made on understanding galaxy mergers since the advent of high resolution computer simulations. Realistic observational comparisons are now becoming easier through the application of observational filter functions, point-spread functions and radiative transfer of starlight through dust, to simulation outputs (e.g. Lotz et al. 2008). However, many areas of parameter space remain relatively unexplored with potentially large implications for our overall understanding of galaxy formation. For example, the comparison between simulations of galaxy mergers with and without mechanical AGN feedback is rarely focused upon, with some groups preferring to focus on starburst feedback, and others on the possible impact of an active nucleus (for an exception, see Khalatyan et al. 2008).

In this paper we compare observational results directly with a suite of smoothed-particle hydrodynamic simulations of galaxy mergers from Johansson et al. (2009), both with and without AGN feedback, by converting the star formation histories of the simulated galaxies into integrated spectra, upon which the same analysis can be performed as upon the observations. Rest-frame optical spectra contain a wealth of information about a galaxy's past and present star formation rate, often referred to as the galaxy "fossil record" (e.g. Panter et al. 2003). In particular, the 4000Å break and Hδ absorption line strengths constrain the specific star formation rate and amplitude of recent bursts of star formation (Kauffmann et al. 2003a). At low redshift, the quality of spectra and models now allow the analysis of large spectral regions (Cid Fernandes et al. 2005; Tojeiro et al. 2007; Wild et al. 2007; Koleva et al. 2008). At high redshift, spectral indices easily separate blue from red sequence galaxies without the complication of dust (Vergani et al. 2008). At these redshifts, where galaxy spectra are in general noisier, modern statistical techniques present us with the opportunity to vastly increase the quantity and improve the quality of derived parameters. Following Wild et al. (2007), this paper presents a principal component analysis of the 4000Å break region of more than one thousand high redshift galaxy spectra culled from the VIMOS VLT Deep Survey (VVDS, Le Fèvre et al. 2005). We use the information encoded in the spectra to recover the recent star formation history of galaxies at an epoch when the Universe was very different from today.

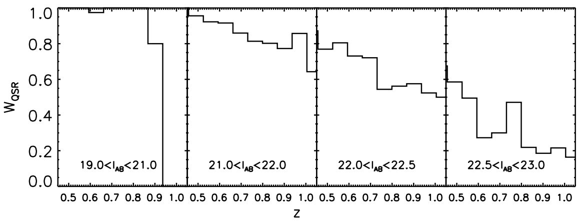

Figure 1. The "quality sampling rate" between $0.5 < z < 1.0$ for a SNR limit of 6.5 and in four bins of I$_{AB}$ apparent magnitude.

From an observational perspective, so-called "transition" galaxies are of significant interest for pinning down which physical processes play the largest role in shaping the evolution of galaxies. Classes of galaxies which could be transitioning between the blue and red sequences are "post-starburst" galaxies (e.g. Tran et al. 2004; Quintero et al. 2004; Le Borgne et al. 2006; Kaviraj et al. 2007) and "green-valley" galaxies (e.g. Martin et al. 2007). From the build up of the red sequence in the VVDS, Arnouts et al. (2007) measured the net mass flux which has taken place from the blue sequence to the red sequence. This amounts to 9.8×10^{-3}M$_\odot$/yr/Mpc^3 for a Chabrier (2003) initial mass function (IMF), or about 1.4×10^4 M$_\odot$/yr in the entire VVDS survey volume. As we shall show in this paper, galaxies which have undergone sudden quenching of star formation can be identified in VVDS spectra for a period of $\sim 0.35-0.6$ Gyr after the quenching event. Therefore, if the entire build up of the red sequence were due to a physical process associated with fast quenching, such as gas rich major mergers, we could expect to identify a net transitioning stellar mass of $6-10\times10^5$M$_\odot$/Mpc^3, or about $8.5-14\times10^{11}$M$_\odot$ in the VVDS survey, after accounting for targeting rates. This could comprise, for example, a few tens of galaxies of stellar mass $\log(\mathrm{M}/\mathrm{M}_\odot) = 10.5$.

The primary questions that we wish to address in this paper are, how much mass do we see entering the red sequence after an episode of fast quenching? Are gas-rich major mergers an important mechanism for the build up of the red-sequence since $z \sim 1$? Section 2 describes the VVDS spectroscopic survey and Section 3 presents our method for identifying post-starburst galaxies. In Section 4 we place our empirical results within a theoretical framework, through comparisons with simple synthesised stellar populations and the star formation histories of galaxy merger simulations. The results are presented in Section 5 and compared to the low redshift Universe in Section 6. In Section 7 we discuss the global importance of post-starburst galaxies for developing a complete picture of the evolution of the galaxy population.

Throughout the paper we assume a cosmology with $H_0 = 70\,\mathrm{km\,s^{-1}\,Mpc^{-1}}$, $\Omega_\mathrm{m} = 0.3$ and $\Omega_\Lambda = 0.7$.

2 THE VVDS DATASET

The VIMOS VLT Deep survey (VVDS) is a deep spectroscopic redshift survey, targeting objects with apparent magnitudes in the range of $17.5 \leqslant I_{AB} \leqslant 24$. The survey is unique for high redshift galaxy surveys in having applied no further colour cuts to minimise contamination from stars, yielding a particularly simple selection function. In this work we make use of $\sim$ 9000 spectra from the publicly available first epoch public data release of the VVDS-0226-04 (VVDS-02h) field which covers an area of 1750 square arcmins (Le Fèvre et al. 2005). The spectra have a resolution (R) of 227 and a dispersion of 7.14 Å/pixel and a useful observed frame wavelength range, for our purposes, of 5500-8500 Å.

The first epoch public data release contains 8981 spectroscopically observed objects in the VVDS-02h field, 8893 of which are within the presently defined survey mask. Of these, 7194 have secure redshifts (flags 2, 3, 4 and 9, see below), are not classified as type 1 AGN and are not secondary objects in the slit. To measure each galaxy's star formation history we require coverage of the rest-frame wavelength range 3750–4140Å, which restricts the redshift range of our galaxy sample to $0.5 < z < 1.0$. As discussed in detail in Section 2.1.3 below, we impose a signal-to-noise (SNR) limit on the spectra greater than 6.5 and magnitude limits of $19 < I_{AB} < 23$, resulting in a final sample of 1246 galaxies.

In addition to the spectra the dataset includes multi-wavelength photometry from diverse sources. Data assembled within the context of the VVDS survey include deep B, V, R, and I photometry from the CFHT/CFH12K camera[1] with limiting magnitudes of 26.5, 26.2, 25.9, and 25.0, respectively (McCracken et al. 2003; Le Fèvre et al. 2004). Further optical photometry from the Canada-France-Hawaii Telescope Legacy Survey (CFHTLS[2]) extends into the u and z bands. The field has deep NIR imaging down to limits of J≈ 21.50 and K≈ 20.75 (Iovino et al. 2005) and NUV and FUV coverage as part of the GALEX mission (Martin et al. 2005). In order to avoid source confusion due to the large point spread function (PSF) of GALEX, UV photometry is based upon optical priors (Arnouts et al., in prep.). Infrared photometry in the IRAC 3.6, 4.5, 5.8 and 8.0 μm is available from the Spitzer Wide-area InfraRed Extragalactic survey (SWIRE, Lonsdale et al. 2003). We use the source catalogue as released by the SWIRE team[3], with detection limits at 5σ of 5.0, 9.0, 43.0, 40.0 μJy, respectively. In this paper the photometric data is used primarily for the purpose of deriving stellar masses, as described in Walcher et al. (2008, see Section 2.2).

2.1 Accounting for unobserved galaxies

In order to calculate absolute quantities from galaxy redshift surveys, such as galaxy numbers and mass densities, it is necessary to account for several effects which cause galaxies not to be included. For our work there are three effects:

- The *target sampling rate* (TSR): only a fraction of all galaxies in the given magnitude range and survey area are targeted for spectroscopic follow-up.
- The *spectroscopic success rate* (SSR): a fraction of targeted and observed galaxies cannot be successfully assigned redshifts, due to either sky line contamination or featureless spectra.
- The spectroscopic *quality success rate* (QSR): only a fraction of the targeted galaxies with successful redshifts have high enough quality spectra from which star formation histories can be measured.

The TSR and SSR are common to many results derived from the VVDS, such as luminosity functions, and are explained in detail in e.g. Ilbert et al. (2005); only the QSR is new to this work.

2.1.1 The Target Sampling Rate (TSR)

As described in Ilbert et al. (2005), in order to maximise the number of targeted objects per VIMOS pointing, the TSR is a function of the size of the galaxy. We obtain the TSR from Figure 1 of Ilbert et al. (2005) and weight each galaxy according to its size $w_i^{\mathrm{TSR}} = 1/\mathrm{TSR}(\mathrm{r_i})$, where r_i is the x-radius parameter of each galaxy.

2.1.2 The Spectroscopic Success Rate (SSR)

The second effect, the SSR, is potentially much more complicated, because the success of obtaining a redshift for a galaxy depends not only on the apparent magnitude of the galaxy, but also on its redshift and spectral type. The rest-frame spectroscopic features which allow accurate redshift determinations depend on the spectral type of the galaxy and move through the observed-frame wavelength range depending on the redshift of the galaxy. In the VVDS each object is assigned a redshift quality flag, which approximates the security of the given redshift. Galaxies with flags 2, 3, 4 and 9 are deemed secure[4]. In order to account for the changing SSR as a function of redshift, and following the method presented in Section 3.2 of Ilbert et al. (2005), we estimate the SSR by making use of the photometric redshifts calculated by Ilbert et al. (2006), which are publicly available through the Terapix Consortium[5]. We calculate the SSR as a function of redshift and magnitude, as the number of objects with secure redshifts (flags 2,3,4,9) divided by the total number of objects (with flags 0,1,2,3,4 and 9). Photometric redshifts are used to place the galaxies without secure spectroscopic redshifts in the correct redshift bin.

We calculate the SSR in 4 bins of apparent magnitude 19–21, 21–22, 22–22.5 and 22.5–23, with bins in Δz_{phot} of width 0.05. Galaxies brighter than 19 and fainter than 23 magnitudes are not used in this work, the former because of our lower redshift limit of $z = 0.5$ and the latter because of the signal-to-noise limitation we place on the spectra as described in the following subsection.

We weight each galaxy in our sample by $w_i^{\mathrm{SSR}} = 1/\mathrm{SSR}(\mathrm{z_{spec}}, I_{AB})$, where z_{spec} is the spectroscopic redshift of the galaxy, and I_{AB} is its I-band apparent magnitude.

It is important that galaxies with different SEDs are treated equally during this weighting procedure. Quiescent galaxies are the hardest to assign redshifts to, due to their lack of emission lines. To check that the completeness for quiescent galaxies is accurately estimated using the SED-independent method described above, we split our sample into high and low SFR subsamples, where SFR was measured from SED fitting to multiwavelength photometry (see Section 2.2). We repeated the calculation of w_i^{SSR} for each subsample and found them to be consistent with each other over the redshift range $0.5 < z < 1$ used in this paper. This redshift range is expected to be the least problematic, due to the coverage of the 4000Å break which is strong in quiescent populations.

2.1.3 The Quality Success Rate (QSR)

The final selection criterium applied to the VVDS galaxies to create the sample studied in this paper is that they have spectra of high enough continuum SNR to allow us to extract useful information on their star formation histories. In practice, this means a median per-pixel-SNR[6] larger than 6.5. The SNR of the observed spectrum depends on both the apparent magnitude of the galaxy, because all galaxies are observed with equal exposure times, and the redshift of the galaxy, because the flux of a galaxy varies with wavelength.

---

[1] http://cencosw.oamp.fr/

[2] http://www.cfht.hawaii.edu/Science/CFHTLS

[3] http://swire.ipac.caltech.edu/swire/swire.html

[4] Flag 9: redshift determined from single emission line; Flag 4: 100% confidence; Flag 3: 95% confidence; Flag 2: 75% confidence (Ilbert et al. 2005)

[5] ftp://ftpix.iap.fr/pub/CFHTLS-zphot-v1/

Thus, in a similar manner as for the SSR, we define the quality success rate (QSR) to be the total number of galaxies with secure redshifts and SNR greater than our limit, divided by the total number of galaxies with secure redshifts (flags 2,3,4 and 9). We calculate this in the same four bins of apparent magnitude used for the SSR and in spectroscopic redshift bins of width $\Delta z_{\rm spec} = 0.05$. We weight each galaxy in our sample by $w_i^{\rm QSR} = 1/{\rm QSR}({\rm z_{spec}}, I_{AB})$. The $w^{\rm QSR}$ is shown in Figure 1 for the four magnitude bins. In Section 5.2 we will show that we recover stellar mass densities consistent with previous work, despite the addition of this new selection criterion.

Imposing a SNR threshold on the data was found to be necessary for this work. Using spectra with too low SNR causes considerable scatter in our spectroscopic indices, which makes difficult the robust identification of the post-starburst galaxies in which we are primarily interested. This problem is easily identifiable: the increased scatter in the indices causes the number of post-starburst galaxies to increase relative to the total sample, and biases the SNR distribution of the candidate post-starbursts towards lower values than typically seen in the population as a whole. Therefore the SNR limit was chosen empirically, by ensuring that the distribution of SNR in our post-starburst galaxy sample was similar to that for galaxies of other types, and that our total completeness-corrected stellar mass densities for each class of galaxy (i.e. quiescent, star forming, post-starburst, starburst) remained constant when the SNR limit was increased by a small amount. We found that a per-pixel-SNR limit of 6.5 was required for the purposes of our study.

2.2 Measuring Stellar masses

A full description of the method used to measure the stellar masses of our galaxies is given in Walcher et al. (2008), to which we refer the reader for details. Briefly, we derive the stellar mass M* for each galaxy by fitting its multi-band UV–IR spectral energy distribution (SED), to model stellar populations created using the (Bruzual & Charlot 2003) population synthesis models, assuming a Chabrier (2003) initial mass function (IMF). We create a library of exponentially declining star formation histories with superposed stochastic top-hat bursts (see Kauffmann et al. 2003 and Salim et al. 2005 for descriptions of similar libraries). The method uses Bayesian probability distribution functions as described in Appendix A of Kauffmann et al. (2003) to derive physical parameter estimates for each observed SED, including errors on the parameters. For a detailed discussion of the accuracy of stellar mass estimates using SED fitting methods see Pozzetti et al. (2007).

2.3 Volume correction

To account for the changing effective survey volume for galaxies of different brightnesses and SED shapes, we use the V$_{\rm max}$ method (Schmidt 1968). This weights galaxies according to the fraction of the survey volume in which they could have been observed, given their brightness and the shape of their SED. The latter point is important: galaxies with different SED shapes are visible in different survey volumes and this must be correctly accounted for in the V$_{\rm max}$ calculation (Ilbert et al. 2004). Using the same library of models as used in the stellar mass determination (see above), the best fit model was scaled to the observed galaxy magnitude and shifted in redshift to determine the total redshift path in which the galaxy would have been seen, given the survey magnitude limits.

The SNR limit alters slightly the effective I_{AB} magnitude limits of the survey, because very few galaxies with apparent magnitudes above 23 have spectra with a SNR greater than our limit of 6.5. We therefore redefine the survey magnitude range to be $19 < I_{AB} < 23$ and remove galaxies from our sample which fall outside of these limits.

2.4 The survey volume

The survey area is calculated from the photometric survey mask, combined with the boundaries of the spectroscopic survey region. The total survey area is 0.472 sq. degrees which corresponds to a survey volume in the redshift range $0.5 < z < 1.0$ of 1.4×10^6 Mpc^3.

3 LOCATING RECENTLY DEAD GALAXIES

The galaxies in which we are interested are those in which a dominant A/F star population is visible, implying that the formation of O and early B type stars has ceased suddenly. Such galaxies are identifiable by their strong Balmer absorption lines compared to their mean stellar age as measured by their 4000Å break strength. The traditional method for identifying post-starburst galaxies involves the selection of objects with both a strong Balmer absorption line (usually Hβ or Hδ) to identify a recent starburst, and no detectable nebular emission (usually [OII] or Hα, although see Balogh & Morris [2000]) to ensure no ongoing star formation. Our selection differs primarily by not placing limits on nebular emission, as we do not want to bias our sample against narrow line AGN which are enhanced in the post-starburst population (Yan et al. 2006; Wild et al. 2007; Schawinski et al. 2007). The additional use of the 4000Å break strength allows us to select galaxies with older and weaker post-starburst features.

Following the method of Wild et al. (2007) we employ a Principal Component Analysis (PCA) of the spectra around the 4000Å break to measure the strength of the Balmer lines with sufficient SNR. In Wild et al. (2007) the new spectral indices were defined based upon stellar population synthesis models to avoid contamination of the indices by gaseous emission from the galaxies. Because of the low spectral resolution of the VVDS spectra, in this work we are unable to accurately mask the Balmer emission lines which fall in the center of the Balmer absorption lines in which we are interested. Therefore, we choose to perform the PCA directly on the VVDS spectra themselves. In Section 4 we explain how we compare a posteriori to model stellar populations created with a population synthesis code.

3.1 Calculating the spectroscopic indices

All galaxy spectra in our sample are corrected for Galactic extinction assuming a uniform E(B−V)$= 0.027$ (McCracken et al. 2003), moved to the galaxy rest-frame and interpolated onto a common wavelength grid. Each spectrum is normalised, by dividing by the median flux between 3750 and 4140 Å. The mean spectrum

---

[6] Per-pixel SNR is calculated from the median flux over error in the wavelength range 5500–8500Å.

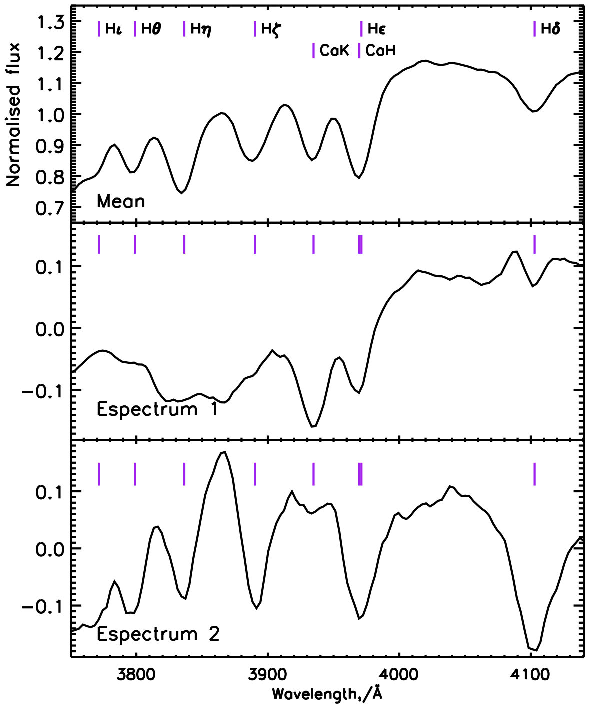

Figure 2. The eigenspectra of the VVDS galaxy sample in the rest-frame wavelength range 3750-4140 Å. The spectral indices used in this paper refer to the amount of each eigenspectrum present in an individual galaxy spectrum. The first index is related to the shape of the spectrum and equivalent to the common D$_n$4000 index. The second index contains the Balmer absorption line series from Hδ to Hθ, together with the distinctive decrease in flux bluewards of 3850 Å seen in late B to F-star spectra.

is calculated and subtracted and a PCA is then performed on the residuals. Because PCA is a least-squares process, eigenspectra calculated directly from data can easily be dominated by outliers in the input sample of spectra. In order to obtain robust eigenspectra that are representative of the majority of the population, we use an iterative and robust PCA algorithm (Budavari et al. 2008). The algorithm essentially replaces the least-squares minimisation solved by traditional PCA with the minimisation of a new robust function of the data, which employs a robust Cauchy-type function to limit the impact of outliers. The eigenspectra are presented in Figure 2. As described in detail in Wild et al. (2007), the first eigenspectrum relates to the strength of the 4000Å break, and is equivalent to the well-known index D$_n$4000. This has been shown to correlate most strongly with the specific star formation rate of the galaxy (SSFR, star formation rate divided by stellar mass, Brinchmann et al. 2004). The second index contains the Balmer absorption lines, together with the correlated decrease in flux bluewards of 3850 Å found in late B- to F-type stars.

We calculate the principal component amplitudes (PCs) of all galaxies in our sample by projecting the spectra onto the eigenspectra. The projection is performed using the "gappy-PCA" procedure of Connolly & Szalay (1999), which weights pixels by their errors during the projection and gaps in the spectra due to bad pixels are given zero weight. We additionally allow the normalisation of the spectra to vary as a free parameter in the projection (G. Lemson private communication, see Wild et al. 2007). The PCs represent the amount of each eigenspectrum present in a galaxy spectrum and are our new star formation history indices. Errors are calculated during the projection of the spectra onto the eigenspectra, using the error arrays of the individual VVDS spectra. These errors are purely statistical, however, in Wild et al. (2007) we show that for SDSS spectra they compare well to the scatter observed between duplicate observations.

3.2 Defining the post-starburst galaxy sample

In Figure 3 we show the distribution of PC1 and PC2 for our sample of VVDS galaxies. To guide the eye of the reader, and to aid in further discussion, we have split the sample into four "classes", with boundaries empirically defined from the distribution of points. We would like to emphasise that in reality the star formation histories of galaxies form a continuous distribution, and any separation into discrete classes is an over simplification, greatly reducing the information contained within the full distribution. The primary division of our sample is into "quiescent" and "star-forming" galaxies on the right and left, based on the value of PC1 (i.e. the strength of their 4000Å break). The precise positioning of the boundary is arbitrary, and care should be taken when comparing our results for "red" and "blue" galaxies to those derived from different observations. To the bottom left, systems with very blue continua and very strong emission lines are found, which we class as "starburst" galaxies.

Finally, to the top center we find the "post-starburst" galaxies, with stronger Balmer absorption lines than expected for their 4000Å break strength. We define "post-starburst" galaxies to have $-0.6 < \mathrm{PC1} < 1.0$ and PC2> 0.6. While these boundaries were defined empirically from the distribution of data (this class are clear outliers in PC2), we will later compare with model stellar populations to justify their classification as "post-starburst". We find that 18 galaxies lie in this region at $> 1\sigma$ confidence. The spectra of these galaxies are shown in Figure 4. The selection of these 18 galaxies is robust to changes in the exact method used to create the eigenspectra.

3.3 Estimating completeness limits

It is important to estimate the completeness of the survey in terms of galaxy stellar mass. This of course depends upon the mass-to-light ratio and SED shape of the galaxies in question: flux limited surveys are generally complete to lower mass limits for star forming galaxies than for quiescent galaxies. While the completeness in a particular photometric band can be judged empirically, this is not possible for the completeness in derived parameters, such as stellar mass and star formation rate. We therefore use an alternative approach to estimate the mass completeness of our sample, described in detail in W08.

Because we are primarily interested in the post-starburst population, with mass-to-light ratios between those of star-forming and quiescent galaxies, we derive the mass limits relevant for this population alone. From the model dataset described in Section 2.2 we select all model galaxies which have undergone a starburst in the last Gyr and lie within our PSB region in PC1/PC2. For a given stellar mass, we determine the fraction of model post-starburst galaxies that lie within our survey magnitude limits. We find that 50% of the model post-starburst galaxies at $z = 0.6$ with $\log(\mathrm{M}/\mathrm{M}_{\odot})> 9.5$ would be detected, and $\log(\mathrm{M}/\mathrm{M}_{\odot})> 9.9$ at $z = 0.9$. The stochastic model library assumed in this analysis has a higher fraction of strong post-starburst galaxies than appear in the real data, i.e. while the observational PC1/PC2 space is fully covered by the models, the relative space density of the different galaxy types is not reli-

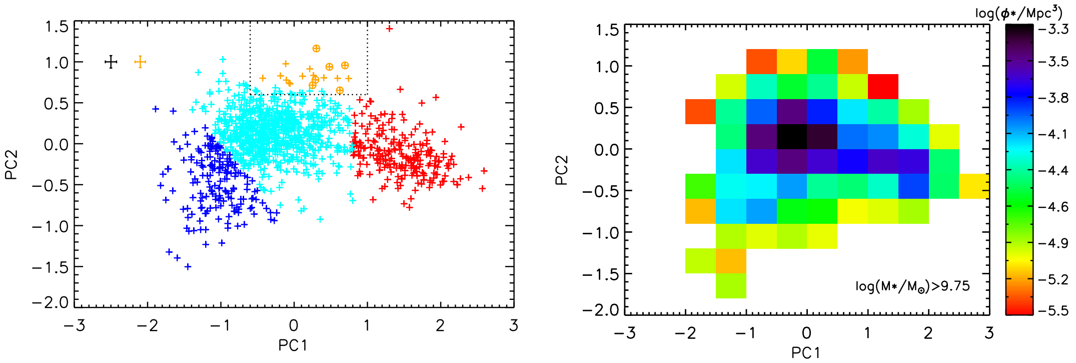

Figure 3. *Left:* The first two principal components (PCs) for all galaxies in our VVDS sample. PC1 is equivalent to the well known index D_n4000, PC2 represents the excess (or lack) of Balmer absorption. For analysis purposes, the sample has been split into quiescent (red), starforming (cyan), star-bursting (blue) and post-starburst (orange) classes. Post-starburst galaxies are defined to lie within the dotted box indicated by at least 1σ. Those with SSFR$< 10^{-11}$/yr are circled. The median errors of the whole sample (black) and the post-starburst galaxies alone (orange) are shown in the top left. *Right:* The volume density of galaxies with $\log(\mathrm{M}/\mathrm{M}_\odot)> 9.75$ in 0.5×0.3 bins in PC1/PC2.

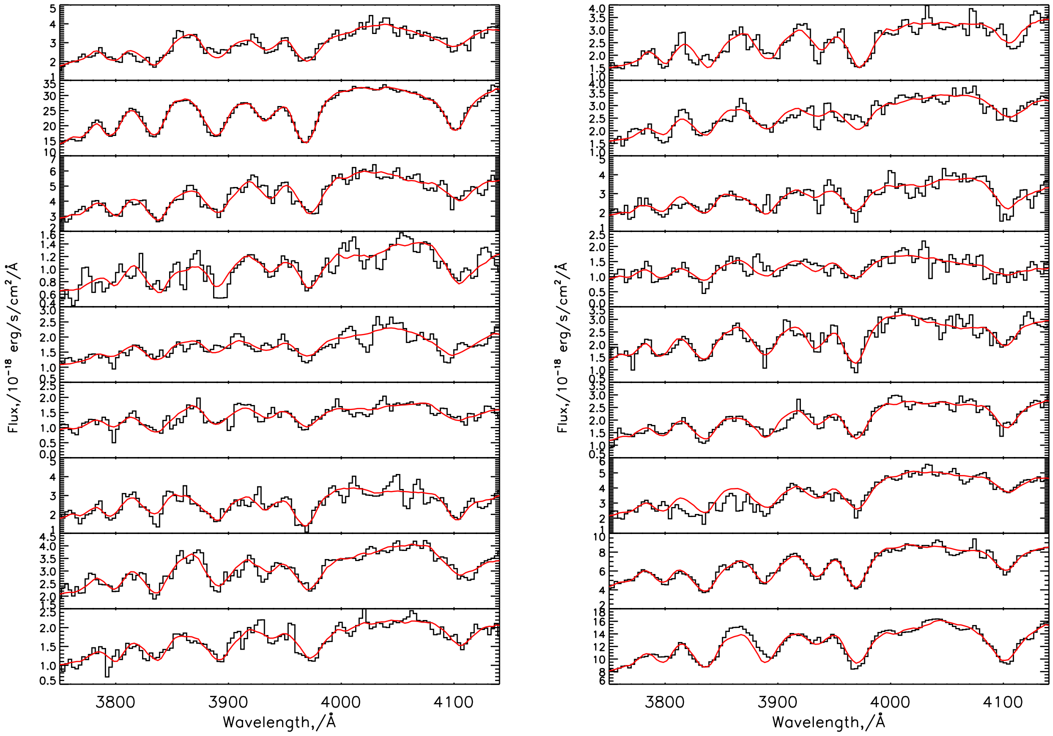

Figure 4. The spectra of post-starburst galaxies culled from the VVDS galaxy sample in the rest wavelength range 3750–4140Å. Overplotted in red are the PCA fits to the spectra using 10 components.

able. We therefore confirmed that the mass completeness limits did not vary greatly with burst mass fraction or burst age.

In the following sections, all results will be quoted for a mass limit of $\log(\mathrm{M}/\mathrm{M}_\odot)> 9.75$. We have confirmed that increasing this limit to $\log(\mathrm{M}/\mathrm{M}_\odot)> 10.0$ does not alter our conclusions. Figure 3 (right) shows the number density of galaxies in bins of PC1/2 for galaxies with $\log(\mathrm{M}/\mathrm{M}_\odot)> 9.75$, corrected for survey volume and sampling effects.

4 COMPARISON WITH MODELS

In order to understand the particular properties of a starburst which would lead to a post-starburst galaxy in our sample, and to measure the timescale during which a post-starburst galaxy is visible, it is necessary to compare our data with model stellar populations. We begin by creating simple toy model starbursts and subsequently turn to the analysis of smoothed particle hydrodynamic (SPH) simulations of merging galaxies.

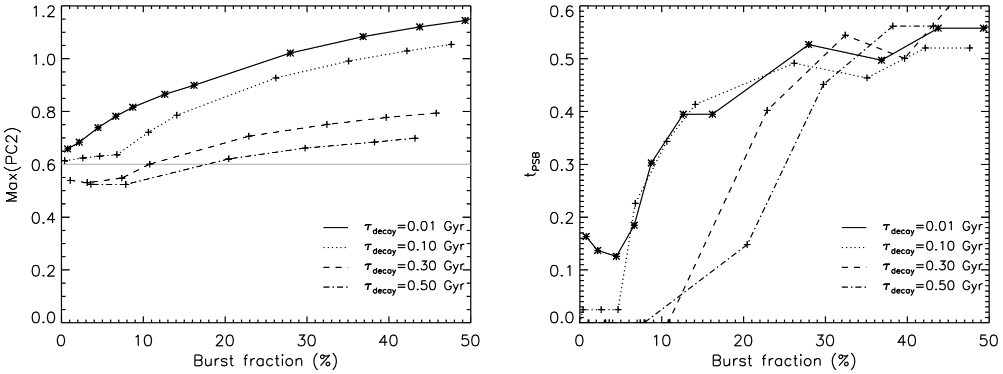

Figure 5. By projecting evolving model stellar populations onto the VVDS eigenspectra, we can measure quantitative properties relevant to our PSB galaxies. After continuously forming stars for 5 Gyr, the toy-model galaxies undergo a starburst which declines exponentially with decay time τ_{decay}. *Left:* The maximum PC2 attained by the models after the starburst has occurred, i.e. a measure of the strength of the PSB features. Different lines represent models with bursts of different τ_{decay}. *Right:* The time spent in the PSB phase as a function of burst mass fraction.

4.1 Toy model galaxy tracks

For a galaxy to reveal strong Balmer absorption lines, star formation must switch off rapidly resulting in an excess of longer lived A- and F-stars over the hotter O- and early B-stars. This does not necessarily have to be preceded by a short-lived starburst, the sudden truncation of ordinary star formation will suffice, although the signature will of course be weaker. The two parameters of importance for the strength and longevity of the post-starburst phase are the mass fraction of stars formed in a starburst and the decay timescale of the starburst. In this terminology, a truncation model then simply has a mass fraction of zero per cent.

With this in mind we have created a library of model galaxies which undergo exponentially decaying bursts, occurring after 5 Gyr of continuous star formation. These bursts are parameterised by their decay time and burst mass fraction, i.e. the mass of stars formed while the star formation rate is above the continuum level.

Converting the star formation histories into spectra suitable for comparison with the VVDS dataset requires several steps. We input the star formation histories into the GALAXEV code (Bruzual & Charlot 2003), using Charlot & Bruzual (in preparation) simple-stellar-populations (SSPs), a Chabrier (2003) IMF and assuming solar metallicity. The evolution of the model galaxies in PC1/2 is not greatly affected by the change between Bruzual & Charlot (2003) and Charlot & Bruzual (in preparation) SSPs, which involves both a change in stellar libraries and in the stellar evolution tracks. Solar metallicity was chosen as being suitable for our post-starburst galaxy sample, given their stellar masses (Section 5.1), but the evolutionary tracks are insensitive to moderate variations in metallicity. The two component dust prescription of Charlot & Fall (2000) is applied to the continuum light as implemented in the GALAXEV code. Again, the inclusion or not of continuum dust has little effect on the time spent on the PSB sequence, or the maximum PC2 observed. This is because the dominant A/F star population in the post-starburst spectra is assumed to already have emerged from the dense stellar birth clouds.

Next, because the resolution of the VVDS spectra is too low to mask emission lines in the data, we must add emission lines to the model spectra. We convert the rate of ionising photons predicted by the stellar population synthesis model (Q_{ion}) into Hα line flux using:

$$F_{H\alpha}[erg/s] = 0.45 * E_{H\alpha}[erg] * Q_{ion}[s^{-1}] \qquad (1)$$

where E$_{H\alpha}$ is the energy of a Hα photon and 0.45 is the fraction of ionisations which lead to the emission of an Hα recombination photon (case B, $\mathrm{Te} = 1 \times 10^4$K and $\mathrm{Ne} = 1 \times 10^4\mathrm{cm}^{-3}$, Storey & Hummer 1995). The remaining Balmer line fluxes are derived from the ratios given in Osterbrock (1989). The stellar population synthesis model includes the post-AGB phase of stellar evolution which is believed to be important for producing ionising photons in older stellar populations (Binette et al. 1994). We note that no contribution to the emission lines from obscured, narrow-line AGN is included in the models. Any substantial infilling of the Balmer absorption lines in this way will prevent us from identifying post-starburst galaxies. AGN with strong enough lines to have a significant effect are extremely rare however, and their absence from our sample will not affect our final results.

Just as dust attenuation is applied to the model stellar continua, the lines are similarly attenuated using the attenuation law as described in Wild et al. (2007):

$$\frac{\tau_\lambda}{\tau_V} = (1-\mu)(\frac{\lambda}{5500\text{Å}})^{-1.3} + \mu(\frac{\lambda}{5500\text{Å}})^{-0.7}. \qquad (2)$$

This law is inspired by the two-component dust model of Charlot & Fall (2000). For the birth clouds, from which nebular emission is believed to originate and which contain a fraction $1-\mu$ of the dust, these authors adopted for simplicity an attenuation law to match that of the diffuse interstellar medium (i.e. of the form $\lambda^{-0.7}$). Our slightly steeper curve, resulting in slightly increased attenuation, is motivated by the fact that dense clouds around young stars have a more shell-like geometry than the diffuse interstellar medium (see da Cunha et al. 2008, for more details). The attenuation of the model emission lines by a moderate amount ($A_V = 1.0$) alters slightly the evolutionary tracks in PC1/PC2 of the model during the starburst phase.

Our ability to detect a post-starburst galaxy depends on the maximum PC2 reached during the evolution of the stellar population, and the time spent in the post-starburst phase (t_{PSB}). These factors depend in turn on the strength of the proceeding starburst, together with the timescale of the subsequent decay of the star formation rate (τ_{decay}). Figure 3 shows that the maximum PC2 reached by the VVDS galaxies is around 1.0, with 5/18 having PC2 >0.9. Using our toy models, the left panel of Figure 5 shows the maximum value of PC2 attained by a model galaxy after the burst has occurred, as a function of the burst mass and burst decay time. The models show that the descendants of starbursts with decay times $\lesssim 0.1$ Gyr and burst fractions above a few percent will appear clearly in the post-starburst phase. The right panel of Figure 5 shows the time spent in the post-starburst phase ($t_{\rm PSB}$). This time is short, $\lesssim$0.15 Gyr, for burst mass fractions < 5%, and reaches a maximum independent of decay time of $\sim$0.6 Gyr for mass fractions of $\gtrsim$30%. We will use this value as an upper limit on $t_{\rm PSB}$ in later sections.

We conclude from this section that the majority of the progenitors of our PSB galaxies underwent a recent strong starburst, followed by a rapid truncation of the star formation. A small fraction may however be simply the result of rapid truncation of their ongoing star formation.

4.2 Simulation galaxy tracks

The next step in our comparison with models involves a sample of 79 merger simulations presented in Johansson et al. (2009, hereafter JNB09).

4.2.1 Simulation details

The simulations were performed using the entropy conserving TreeSPH-code GADGET-2 (Springel 2005), which includes radiative cooling for a primordial mixture of hydrogen and helium together with a spatially uniform time-independent local UV background. Star formation and the associated supernova feedback is implemented using the sub-resolution multiphase model developed by Springel & Hernquist (2003). We model the feedback from black holes following the effective subresolution model of Springel et al. (2005b), in which the unresolved accretion onto the black hole (BH) is related to the resolved gas distribution using a Bondi-Hoyle-Lyttleton parameterization (Bondi & Hoyle 1944). Further details concerning the feedback implementations and parameter choices can be found in JNB09. In addition, for the purposes of this paper a new suite of simulations was performed in which the BH feedback was switched off. Such a comparison is important because the BH feedback can cause star formation to completely shut down after the merger, which may plausibly affect both the time the merger remnant spends in the PSB phase, and the strength of the post-starburst features.

The simulations include mergers of gas-rich disks (Sp-Sp), of early-type galaxies and disks (E-Sp, mixed mergers), and mergers of early-type galaxies (E-E, dry mergers). The progenitor galaxies have a range of virial velocities, $v_{\rm vir}$ of 80, 160, 320 and 500 km/s, which determines their masses and sizes (see Eqs. 1 & 2 in JNB09). All model galaxies contain an exponential disk (d) component, together with a stellar bulge (b) embedded in a dark matter halo modelled with the Hernquist (1990) profile. The stellar bulge has a fixed mass ratio of $M_{\rm b}^* = 0.01367 M_{\rm vir} = 1/3 M_{\rm d,tot}$, where the total disk mass is a sum of the disk stellar and gas mass $M_{\rm d,tot} = M_{\rm d}^* + M_{\rm d,gas} = 0.041 M_{\rm vir}$, the disk stellar mass is $M_{\rm d}^* = 0.041(1-f_{\rm gas})M_{\rm vir}$, and $M_{\rm vir}$ is the virial mass of the galaxy. The initial gas fraction $f_{\rm gas}$ takes values of 0.2, 0.4 and 0.8. The galaxies approach each other on parabolic orbits, which are generally motivated by statistics from N-body simulations (Khochfar & Burkert 2006). The resulting merger remnants have total stellar masses between $\log({\rm M}/{\rm M}_\odot) = 9.5 - 12.5$. Both major (1:1) and minor (3:1) mergers were simulated with varying orbital and initial disk geometries (Naab & Burkert 2003). All simulations were evolved for a total of $t = 3$ Gyr, with the merger taking place after approximately 1.5 Gyr, using the local Altix 3700 Bx2 machine hosted at the University Observatory in Munich. In this paper we will primarily concentrate on mergers with prograde in-plane orbits ("G0", i.e. the galaxies collide directly edge on Naab & Burkert 2003). We will additionally show an example in which galaxies rotate in a retrograde sense, with the disks tilted by 30 degrees with respect to one another ("G7"). We will focus exclusively on the Sp-Sp mergers, as all other pair combinations were found not to produce the strength of PSB galaxy visible to us in the data.

As the simulations, and thus star formation rates, are only computed over a total duration of 3 Gyr, we must assume a star formation history and galaxy age for the initial build up of stellar mass in each progenitor galaxy. We assume that by the start of the simulation each galaxy has built both its bulge and disk stellar mass through an exponentially declining star formation rate: ${\rm SFR} = {\rm SFR}_0 + n\exp(-t/\tau)$ where $\tau = 1{\rm Gyr}$. ${\rm SFR}_0$ is the initial SFR of the simulation i.e. $\sim$1.5 Gyr before the merger takes place. n is defined such that the galaxies are 5 Gyr old at the start of the simulation, i.e. the stellar populations are approximately 7.5 Gyr old at the onset of the merger. Both progenitors in a simulation are assumed to undergo the same initial SFH. We note that any similar star formation history can be assumed with which to build the pre-merger galaxies, without significantly affecting their evolution in the post-merger post-starburst phase. The creation of the spectra from the SFHs of the simulations follows exactly the same method as for the toy burst models.

4.2.2 Post-starburst galaxies in merger simulations

Figure 6 shows the star formation history and evolutionary tracks in PC1/2 for three of the major merger simulations with $f_{gas} = 0.2$ (left) and 0.4 (right), BH feedback and prograde, edge-on orbits ("G0") over the 3 Gyr of the simulation. From top to bottom panel the mass of the progenitor galaxies increases. The SFHs of the major merger simulations in general follow similar patterns, with an initial weak enhancement in their star formation, quickly followed by the starburst and decay to zero star formation.

We parameterise the simulations using two simple values to describe the evolution of the starburst. Firstly, the burst mass fraction $f_{\rm burst}$, defined as the mass of stars formed while the SFR is at least 1.05 times the continuum rate, divided by the total mass of the final merger remnant. The continuum rate is measured in the first Gyr of the simulation, and linearly extrapolated across the subsequent starburst. The second parameter is the decay time of the starburst, $t_{\rm decay}$, defined to be the time from the peak of the starburst until the SFR is only 10% of the maximum burst height. These values are shown in the top left of each SFH panel in Figure 6. As found using the toy-models, higher gas fractions lead to stronger post-starburst features and longer periods of time spent in the post-starburst phase.

Using this suite of simulations we can investigate several other initial conditions which affect the evolution of the stellar population of the merger remnant: progenitor mass ratio; orbital geometry; presence or absence of a black hole. We illustrate the latter two in Figure 7. The left two panels show the star formation history and evolutionary tracks in PC1/2 for galaxies with tilted orbital configurations and $f_{gas} = 0.2$. Comparing to the left panels of Figure 6 we see that in this particular suite of simulations, only the prograde edge-on mergers give rise to post-starburst features. While the starbursts are weaker in the other orbital configurations, it is likely that the main cause of the difference is in the longer decay

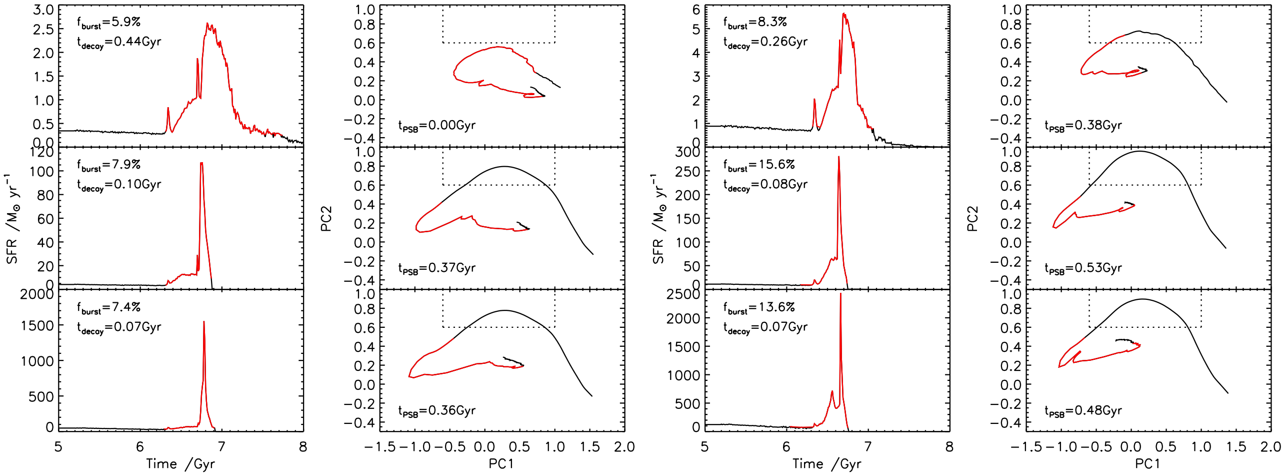

Figure 6. *Far left:* The combined star formation history of both galaxies participating in a major merger during the 3 Gyr SPH simulation. In these panels, the galaxies collide in a "G0" orbital configuration and BH feedback is included. Progenitor galaxies have gas fractions of 20% and virial velocities of 80 (top), 160 (middle) and 320 (lower) km/s corresponding to stellar masses of around 10^{10}, 10^{11} and $10^{12}\mathrm{M}_{\odot}$. The red part of the SFH depicts the "starburst" phase, defined to be where the SFR is 5% greater than the continuum SFR. The values in the top left of the panels are the mass fraction of stars formed during the starburst and the decay timescale of the starburst (see text). *Next left:* the corresponding evolutionary tracks in PC1/PC2, with the red section corresponding to the red section in the left panel. The dotted box shows the PSB region defined in this paper. The time that the merged galaxy spends in the PSB phase is given in the bottom left of the panels. *Right pair of panels:* The same as the left panels, but for progenitor galaxies with gas fractions of 40%.

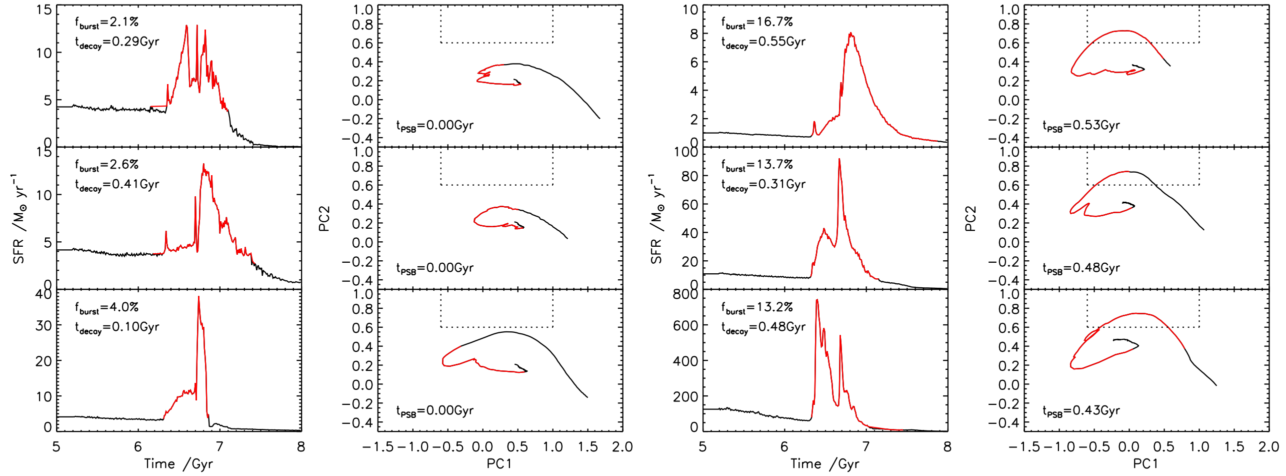

Figure 7. Same as for Figure 6 but for different initial conditions. *Left pair of panels:* Simulations in which the progenitor galaxies collide with inclinations other than edge-on. From top to bottom the orbits are "G7", "G10" and "G13". The galaxies have gas mass fractions of 20% (compare to left hand panels of Figure 6. *Right pair of panels:* Simulations in which the black hole feedback has been switched off. The progenitor galaxies have gas mass fractions of 40% (compare to right hand panels of Figure 6).

times of the star formation rate. However, we caution that the tilted orbital geometries tested here have typical tilts of $\gtrsim 30$ degrees and are retrograde. Other relevant parameters, such as impact parameter, galactic structure and variations in stellar feedback prescription have not been investigated. While the simulations indicate that a relatively strong interaction is required to produce a post-starburst galaxy (see also Cox et al. 2008, JNB09), a full study of the post-merger stellar populations as a function of impact geometries is beyond the scope of this paper.

The right two panels of Figure 7 show the evolution of the stellar population with BH feedback "switched-off" and $f_{gas} = 0.4$. Comparing to the right-hand panels of Figure 6 we see that the burst mass fractions and time spent in the post-starburst phase are similar with or without the presence of BH feedback. The primary causes of the shut-down in star formation are supernovae feedback and exhaustion of gas supplies, rather than any additional energy supplied by the AGN. In two out of three cases the post-starburst features are stronger when BH feedback aids in expelling the gas, but the main effect is focused on the later stages of the burst where any residual star formation is halted more quickly. Therefore, we conclude that from these spectral indices alone, there is no way to confirm or refute the suggestion that strong BH feedback provides the mechanism for shutting off star formation in the Universe.

In Figure 8 we summarise the results by showing the time spent in the post-starburst phase and maximum value of PC2 reached after the merger has occurred, for all of the Sp-Sp merger

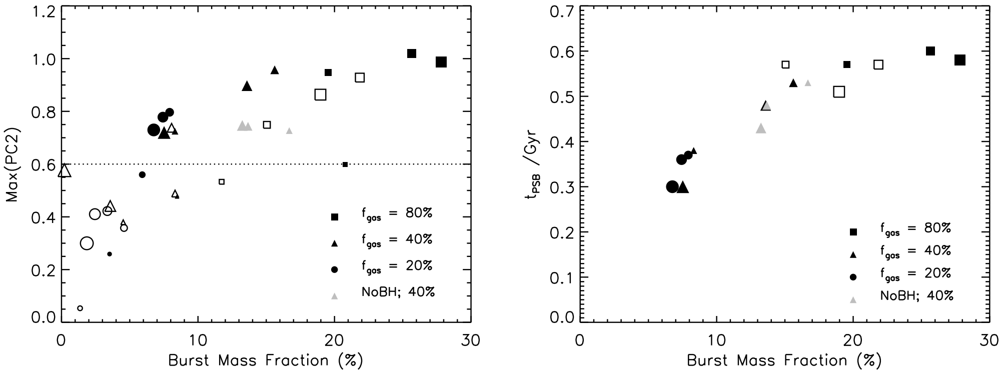

Figure 8. Same as Figure 5 except for SPH galaxy merger simulations with "G0" orbits. Different shapes represent different gas fractions of the progenitor galaxies, filled symbols are 1:1 mass ratio mergers and open symbols are 3:1 mass ratio mergers. Increasing symbol size denotes increasing stellar mass. Gray symbols are mergers with black hole feedback "switched-off", 40% gas fractions and $\upsilon_{\rm vir} = 80$, 160 and 320 km/s. *Left:* The maximum PC2 attained by the models after the starburst has occurred, as a function of burst mass fraction. The dotted line indicates our observational limit above which PSBs are detected. *Right:* The time spent in the PSB phase.

simulations with prograde in-plane orbits ("G0", i.e. directly edge on). The results paint a very similar picture to that shown by the toy-models, but we can now associate burst mass fractions to physically meaningful parameters such as gas fractions and galaxy masses. We find that mergers must induce burst mass fractions of at least 5% for them to be detectable in our observationally defined PSB phase, and the time spent there is greater for more gas rich and more massive mergers. For a 3:1 merger (open symbols) to appear in the PSB phase, a very high gas fraction of 80% is apparently required. The duration of the post-starburst phase tends to a maximum of 0.6 Gyr, with lower gas fractions leading to shorter timescales of 0.3-0.4 Gyr and burst mass fractions of 5-10%. Similar to the toy models, we find that decay times of the starburst must be shorter than ∼0.3 Gyr for a post-starburst galaxy to be observed. The results of three simulations with BH feedback "switched-off", $f_{gas} = 0.4$ and a range of virial masses, are shown as grey symbols. These can be compared directly to the filled triangles in the same figure, in which BH feedback has occurred. We note that the burst mass fractions and starburst decay timescales derived in this section are the same as those found for luminous infra-red galaxies (LIRGS, Marcillac et al. 2006).

Many of the simulated galaxy mergers in the full library of 79 simulations do not result in a post-starburst remnant according to our demanding observational criteria. Even for gas rich major mergers, the starbursts can occasionally be weak and/or have long decay times, thus not creating the sharp discontinuity in SFR required for them to appear in the post-starburst phase. Such galaxies may enter the red sequence through the "green valley" if their star formation rate continues to decay.

5 MASS DENSITIES AND MASS FLUXES OF POST-STARBURST GALAXIES AT Z∼0.7

In the preceding sections we have culled a sample of post-starburst galaxies with $0.5 < z < 1.0$ from the VVDS redshift survey. Through comparisons with toy models and SPH galaxy merger simulations, we have shown how the spectroscopic features indicate that the galaxies have undergone a recent major, gas rich merger. In this section, we will place the post-starburst galaxies into a global context, in terms of their stellar masses, star formation rates and their number and mass densities. Finally, we will address the interesting question: how much mass enters the red sequence through the post-starburst phase?

5.1 Photometrically derived physical properties

We can now ask how the mass of the post-starburst galaxies compares to that of the blue- and red-sequence galaxies? Figure 9 shows the mass distributions of our different classes of galaxies, before and after corrections for sample selection (TSR, QSR and SSR) and survey volume. The galaxies have been classified according to their spectral types i.e. position in PC1/PC2. For clarity, we have combined the starburst and starforming galaxies into a single class; their mass distributions are very similar. The left hand panel shows the mass distribution before correcting for completeness effects. The right hand panel shows the completeness corrected mass distribution, indicating that the post-starburst galaxies primarily have $\log(\mathrm{M}/\mathrm{M}_\odot) < 10.5$, i.e. to the lower end of galaxies in the red sequence and with a similar distribution to galaxies on the blue sequence. It is also worth noting that the completeness corrected mass distribution of the post-starburst galaxies continues to rise to lower masses, and does not turn over before we reach the completeness limit of the sample. Deeper spectroscopic surveys will be required to fully probe the mass distribution of post-starburst galaxies.

Our spectroscopic analysis has focused on uncovering the special class of post-starburst galaxies, and not on recovering further physical parameters. As described in Section 2.2 and more fully in W08, the multiwavelength (UV–IR) SEDs of these galaxies have been analysed to obtain more physical properties than just stellar mass. In Figure 10 we present the light-weighted mean stellar age, specific star formation rate (SFR/M*), time of last burst and dust content of our full sample of galaxies, classified by their PC1/PC2 values. Overall, the relative agreement between the SED fitting and VVDS spectral fitting is remarkable: galaxies which are spectroscopically classified as starforming are found, from multiwavelength photometry, to be younger, have high star formation rates, more recent starbursts and higher dust contents compared to galaxies spectroscopically classified as quiescent. The multiwavelength photometry is able to distinguish that the post-starburst galaxies have ages and star formation rates intermediate between the quiescent and star-forming galaxies. Additionally, the estimated

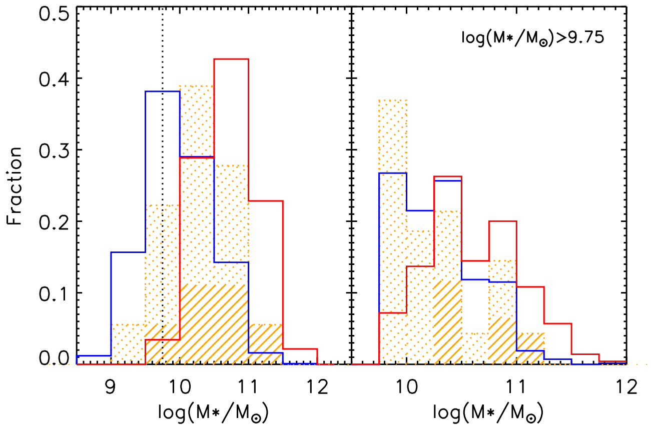

Figure 9. The mass distribution of galaxies, classified into starforming (blue), quiescent (red) and post-starburst (orange, dot-filled) by their spectral type i.e. their PC1/PC2 values shown in Figure 3. The orange line-filled histograms indicate the subset of post-starburst galaxies with no ongoing residual star formation. The verticle dotted line indicates our post-starburst mass completeness limit. *Left:* the raw data, with no correction for survey incompleteness effects. *Right:* for galaxies with stellar masses above our completeness limit, after correction for survey incompleteness effects.

time of their last starburst has a lower mean value than quiescent galaxies, peaking at 10^8–10^9 years, exactly as expected from the VVDS spectral analysis. We can see that the post-starburst galaxies, identified purely through their stellar continuum as having undergone a recent starburst, have a range of specific star formation rates which place them at the lower end of the star-forming sequence through to the quiescent galaxies. In Section 5.3 we will use this result to set a lower limit on the mass flux onto the red sequence through the PSB phase, by identifying those galaxies which have completely ceased star formation.

5.2 Mass and number density

Summing up all the galaxies in our sample above the mass completeness limit of $\log M = 9.75$ with the appropriate weightings, we obtain a total stellar mass density of $\log \rho^* = 8.23^{+0.013}_{-0.011}$. The errors account for individual errors on the stellar masses and Poisson errors from the SSR and QSR weights. As we have placed a stringent criterion on the minimum signal-to-noise ratio of the spectra, it is important to ensure that we recover the correct total stellar mass density found in other work. Pozzetti et al. (2007) calculate the total mass density of galaxies as a function of redshift in the VVDS spectroscopic sample, using the same Chabrier (2003) IMF as used in the present work. Integrating a Schechter function with the parameters[7] given by Pozzetti et al. for the redshift range $0.7 < z < 0.9$ above our mass limit of 9.75 gives a stellar mass density of $\log \rho^* = 8.28$. Although the statistical errors are always $< 10\%$, Pozzetti et al. quote a typical scatter between different methods of mass determination and luminosity function estimates of at least ~ 0.1dex. Taken together with the slightly different redshift range, our results appear to be entirely consistent with those of Pozzetti et al..

Table 1 gives the mass and number densities for each of our galaxy classes. Note that the completeness of our survey is lower for quiescent galaxies than for other classes.

Focussing on the post-starburst galaxies, we find a number density of of 1.0×10^{-4} per Mpc^3 and mass density of $2.69 \times 10^6 \mathrm{M}_\odot/\mathrm{Mpc}^3$. It is instructive to compare their number density to other objects considered to be unusual in the Universe at these redshifts. The number density of our post-starburst sample is 0.3-0.5dex above the number density of powerful X-ray selected AGN with 2-8 KeV luminosities above 10^{43}erg/s at redshifts $0.5 < z < 1.5$ (Barger et al. 2005). They are are factor of 10 more numerous than star-forming galaxies at these redshifts with radio luminosities similar to local ultra luminous infra-red galaxies (ULIRGS, Cowie et al. 2004). The post-starburst galaxies are considerably more common than sub-mm selected galaxies with FIR luminosities $\gtrsim 6 \times 10^{11} \mathrm{L}_\odot$ at $z \sim 0.9$, which have number densities of 3×10^{-6}/Mpc^3/decade (Chapman et al. 2005). These comparisons are designed for orientation only, and not to imply evolutionary sequences: the very different duty cycles and "on" times for different classes of rare objects make inferences about the relation between them difficult. We will return to a quantitative comparison with QSO number densities and major merger rates in Section 7.

5.3 The mass flux of post-starburst galaxies onto the red sequence

We are interested in how much mass may enter the red sequence after a starburst and subsequent fast quenching of the star formation as seen in simulations of major mergers. We estimate the total mass flux which passes through the post-starburst phase to be:

$$\dot{\rho}_{A\rightarrow Q,PSB} = \frac{1}{t_{PSB}} \sum_{i=1}^{N_{PSB}} \frac{M_i^*}{w_i.V_{max,i}} \tag{3}$$

where M^* is the stellar mass of the galaxy in solar masses, w is the combination of the selection functions w^{SSR}, w^{TSR} and w^{QSR}, and V_{max} is the correction for the volume in which each galaxy can be seen. The sum is over post-starburst galaxies above the mass completeness limit of $\log(\mathrm{M}/\mathrm{M}_\odot) > 9.75$. t_{PSB} is the time that a galaxy will be seen in the post-starburst phase. From Section 4 we find t_{PSB} to be less than 0.6 Gyr. Galaxy mergers with lower gas fractions of around 20-40% result in slightly smaller burst mass

---

[7] We compare to the I-band selected sample with masses determined from complex star formation histories (row 7 of their Table 2), for better comparison with our own sample and masses

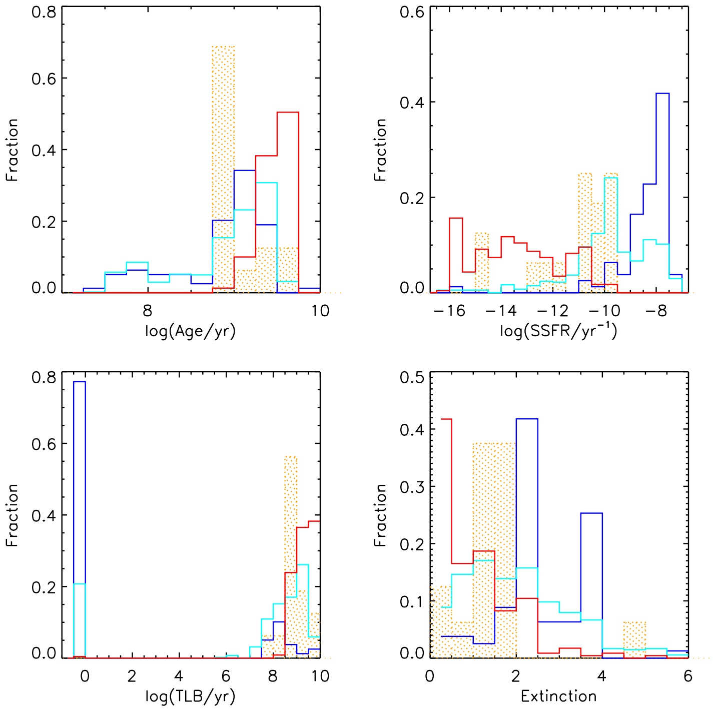

Figure 10. The physical properties of our spectroscopic galaxy sample above a mass limit of $\log(M/M_\odot) > 9.75$, derived from fitting their multiwavelength SEDs (see Walcher et al. 2008). From top left, clockwise: the light-weighted mean stellar age; the specific star formation rate (SFR/M*); the time of the last starburst; the extinction in the V band. The galaxies have been classified by their PC1/2 values into quiescent (red), starforming (cyan), starburst (blue) and post-starburst (orange). The histograms represent the raw data, they are not corrected for incompleteness effects.

Table 1. The mass and number densities of each of our classes of galaxies, for a mass limit of $\log(\mathrm{M/M_\odot}) > 9.75$.

Class	Quiescent	Star-forming	Starburst	Post-starburst	Total
$\log(\mathrm{Number/Mpc^3})$	-2.5	-2.9	-3.1	-4.0	-2.3
$\log(\rho^*/\mathrm{M_\odot/Mpc^3})$	$7.89^{+0.01}_{-0.01}$	$7.88^{+0.02}_{-0.02}$	$7.17^{+0.03}_{-0.04}$	$6.43^{+0.06}_{-0.04}$	$8.23^{+0.01}_{-0.01}$

fractions and shorter time spent in the post-starburst phase of ~ 0.35 Gyr.

During the selection of our post-starburst galaxy sample, we have imposed no restrictions on nebular emission line strengths (see Section 3). However, galaxies which show post-starburst signatures as well as nebular emission lines may be in the process of regenerating their star formation and may therefore subsequently return to the blue-sequence. In order to derive a firm lower limit on the mass flux entering the red sequence through the PSB phase, we elect to sum only those post-starburst galaxies which show no evidence of star formation. Inspecting the distribution of SSFRs of our post-starburst galaxies (top right panel of Figure 10) shows the majority have SSFRs similar to the lower end of the star-forming sequence, 6 objects have SSFRs below 10^{-11} per yr, 5 of which lie above our mass completeness limit. We note that these galaxies also have no measurable [OII] emission. The mass distribution of these galaxies is indicated in Figure 9 by the filled-line histogram and their positions marked in PC1/2 by the open circles in Figure 3.

Summing Equation 3 over the 5 post-starburst galaxies above the mass completeness limit with negligible ongoing star formation as derived from their SEDs, assuming an upper limit for t_{PSB} of 0.6 Gyr, results in a lower limit on the mass flux entering the red sequence through the post-starburst phase of $\dot{\rho}_{A\rightarrow Q,PSB} > 0.0022^{+0.0002}_{-0.006}$ M$_\odot$/Mpc^3/yr. Our best estimate for the mass flux through the post-starburst phase onto the red sequence, assuming $t_{PSB} = 0.35$Gyr, is $\dot{\rho}_{A\rightarrow Q,PSB} = 0.0038^{+0.0004}_{-0.001}$ M$_\odot$/Mpc^3/yr. We note that this is still a lower limit, as we have excluded all those post-starburst galaxies with detectable levels of ongoing star formation. This residual star formation may still decay as the post-starburst ages, we note that the younger post-starburst galaxies (those with smaller PC1) are found to be more likely to have residual star formation than older post-starburst galaxies (see circled points in Figure 3). If all the post-starburst galaxies were to enter the red sequence, for $t_{PSB} = 0.35$Gyr the mass flux would be $\dot{\rho}_{A\rightarrow Q,PSB} = 0.0077$ M$_\odot$/Mpc^3/yr

To determine how important this mass flux is in terms of the global build up of the red sequence, we compare to Arnouts et al. (2007). They use the multiband photometric data in the same VVDS-02h field to measure the mass build up of the red sequence; comparison with this result thus limits our exposure to cosmic variance. The galaxy masses are measured using the same code and model dataset as in this paper, thus eliminating one more potential source of systematic error. They find[8] a total mass growth of the red sequence of $\dot{\rho}_{A\rightarrow Q} = 0.0098$ M$_\odot$/Mpc^3/yr. If we assume that all galaxies that enter the red sequence subsequently remain on the red sequence, then our results show that $> 22^{+2}_{-6}$% and likely as much as 38^{+4}_{-11}% of the growth of the red sequence at $z < 1$ takes place from galaxies which have passed through the strong post-starburst phase. If all our PSB galaxies with $\log(\mathrm{M/M_\odot}) > 9.75$ enter the red sequence, they account for $\sim$ 80% of the growth of the red sequence. We note that these numbers are significant, and perhaps even surprisingly high. We will return to this point in Section 7.

The quoted errors on our mass flux include errors on the individual galaxy stellar masses, calculated from the probability distribution function resulting from the Bayesian SED fit, and the Poisson errors on the QSR and SSR weights. As described in Pozzetti et al. (2007), systematic errors caused by the methods used to estimate the masses and selection of samples lead to a typical scatter in stellar mass densities of 0.1-0.2 dex. If we discard our statistical errors, and assume instead a fixed 0.15 dex error on the stellar mass density of the post-starburst galaxies, we find $\dot{\rho}_{A\rightarrow Q,PSB} = 0.0038^{+0.001}_{-0.002}$ M$_\odot$/Mpc^3/yr. However, our comparison with the results of Arnouts et al. (2007) should be more robust due to the use of the same stellar masses, similar survey selection criteria and survey area.

6 COMPARISON AT LOW REDSHIFT

To create a comparison sample at low redshift, we combine the Sloan Digital Sky Survey (SDSS) spectroscopic data release 5 (DR5, Adelman-McCarthy & et al. 2007) with the UKIRT Infrared Deep Sky Survey (UKIDSS, Lawrence et al. 2007) large area survey (LAS), data release 3 (Warren et al. in prep.). The SDSS DR5 galaxy catalogue (Strauss et al. 2002) covers 5740 sq. degrees and contains more than 670,000 spectra of galaxies with a median redshift of $z \sim 0.1$ and $r_{\mathrm{AB}} < 17.77$. The accompanying SDSS photometric survey provides optical $ugriz$ photometry for each object. UKIDSS is an ongoing survey using the UKIRT Wide Field Camera (WFCAM, Casali et al. 2007) to obtain YJHK near-infrared photometry covering 4000 sq. degrees in the same region of the sky as the SDSS survey. The photometric system is described in (Hewett et al. 2006), the pipeline processing and science archive are described in (Hambly et al. 2008). The LAS reaches a depth in K of 18.4.

For the purposes of this paper, the SDSS provides the spectroscopic data required to locate the post-starburst galaxies, and the near-infrared photometry of the UKIDSS survey is combined with the optical photometry of SDSS to obtain accurate stellar masses. Requiring the objects to be detected in all YJHK bands gives a combined survey area of 916 sq. degrees (S. Maddox, private communication).

6.1 Sample selection and incompleteness corrections

We select SDSS galaxies to have extinction corrected r-band petrosian magnitudes $r_{\mathrm{AB}} < 17.7$, be primary galaxy targets (PRIMTARGET = TARGET_GALAXY or TARGET_GALAXY_BIG or TARGET_GALAXY_RED), primary catalogue objects ($mode = 1$) and spectroscopically classified as a galaxy (SPECCLASS=2). They are matched to UKIDSS galaxies by identifying the closest object within 0.5 arcsec. We remove a small fraction of galaxies (3%) with bad spectra by imposing a per-pixel-SNR limit of 5, and account for this loss in our weighting scheme. Our final sample contains 14822 galaxies with $0.05 < z < 0.1$.

The redshift range is selected with two things in mind. Firstly, we require low enough redshift that our sample is complete down to similar masses as for the VVDS survey and secondly, we require high enough redshift to minimise the aperture bias effect caused by the 3” SDSS fibres. This latter property of the SDSS survey means that the spectra only probe the central regions of nearby, or massive, galaxies, with a strong redshift dependence. For our comparative census of post-starburst galaxies this is problematic as there is currently no known way to robustly detect post-starburst features from optical photometry alone. Thus, it is not possible to know for sure whether the proceeding starburst was nuclear or global, the former being unlikely to be connected to the build up of the red sequence. At $z = 0.05$ the fibre corresponds to a physical diameter of about 3 kpc ($h = 0.7$), which is small compared to the size of a galaxy, but is considerably larger than the extent of a nuclear starburst (Böker et al. 2004). A remaining limitation caused by the aperture bias of SDSS, is that post-starburst populations may fail to be identified due to population gradients within the galaxies. Assuming disks are more likely to undergo starbursts than bulges, this would cause us to underestimate the number of PSB galaxies.

Volume corrections and stellar masses of the galaxies are measured in the same way as for the VVDS sample (Section 2.3), using the combined UKIDSS and SDSS photometry. One final piece of information required is the target sampling rate of SDSS. Although the SDSS aims for 100% coverage in the spectroscopic catalogue, one of a pair of neighbouring galaxies is occasionally not targeted, due to the problem of placing fibres close together on a plate. Similarly, densely populated regions of the sky may suffer from partial coverage due to there being insufficient fibres available to cover the area. For the purposes of this study, we only require the probability that a galaxy was targeted for spectroscopic follow-up, and no further spatial information. We use the SDSS Catalogue Archive Server (CAS) to count the number of galaxies within SDSS spectroscopic sectors that are targeted for spectroscopic follow-up, and the number with spectroscopic ID numbers (i.e. that were targeted). We find that the targeting success rate is 90%. We calculate weights for the galaxies by combining this value with the fraction with spectra above the SNR limit described above.

6.2 Calculating the Principal Components

To calculate the Principal Components for the SDSS spectra, we first correct for Galactic extinction, convert to air wavelengths, convolve the spectra to VVDS resolution and finally rebin onto the eigenspectra binning. We then proceed as for the VVDS spectra (Section 3.1), to obtain the PCs for the SDSS galaxies. The distribution of the first two components is shown in Figure 11. The left panel shows the full sample, and the right panel only galaxies with $\log(\mathrm{M/M_\odot}) > 9.75$. Comparing with Figure 3 there are clear differences between the SDSS and VVDS populations. Firstly the tight blue sequence in SDSS contrasts greatly with the cloud in the VVDS sample. In part this is due to the smaller errors on the spectral indices, but it may also be due to a more “quiescent” mode of star formation in galaxies at low redshifts. The second noticeable difference is that the entire population is older (larger PC1). Fi-

---

[8] They quote a value of $\dot{\rho}_{A\rightarrow Q} = 0.017 \pm 0.004$ M$_\odot$/Mpc^3/yr assuming a Salpeter IMF, to which they convert their Chabrier IMF stellar masses by adding 0.24 dex. Removing this correction results in the value quoted.

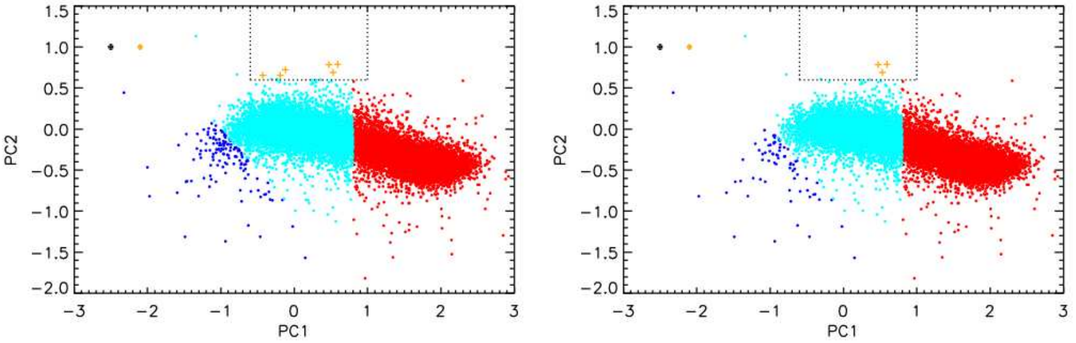

Figure 11. The first two principal components (PCs) for all galaxies in our SDSS sample (left) and for those galaxies above our mass completeness limit, $\log(\mathrm{M}/\mathrm{M}_{\odot}) > 9.75$ (right). For analysis purposes, the samples have been split into quiescent (red), starforming (cyan), star-bursting (blue) and post-starburst (orange) classes. These classes are defined in the same way as for the VVDS sample, except for the positioning of the partition between quiescent and active galaxies (see Fig. 3). The median errors of the whole sample (black) and the post-starburst galaxies alone (orange) are indicated in the top left.

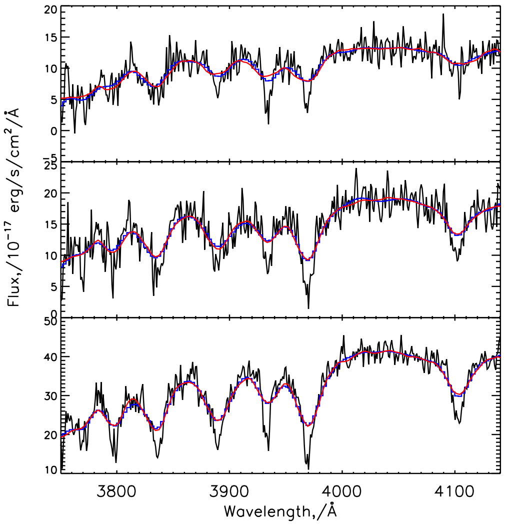

Figure 12. The spectra of post-starburst galaxies culled from the SDSS galaxy sample. The original SDSS spectrum is shown in black, with the convolved spectrum in blue (histogram). The red line is the overplotted fit of the VVDS derived eigenspectra to the SDSS spectra.

nally, we can see that there are fewer strong post-starburst galaxies, despite the enormous increase in overall sample size.

6.3 Mass density of post-starburst galaxies at $z \sim 0.07$

We identify 6 post-starburst galaxies using the same criteria as for the VVDS sample, although from Figure 11 these are clearly only the tip of a distinct and identifiable population. The spectra of the three post-starburst galaxies above the mass limit of $\log(\mathrm{M}/\mathrm{M}_{\odot}) > 9.75$ are shown in Figure 12. The SDSS sample has a high mass completeness even below this mass limit, but for the purposes of comparison we retain the same mass limit as for the VVDS dataset. The number density of PSBs at $z \sim 0.07$ is 5.1×10^{-7}, i.e. a factor of 200 lower than in the VVDS survey at $z \sim 0.7$. For comparison, over the same redshift range the number density of ultra-luminous infrared galaxies (ULIRGs) decreases by a factor of ∼30 (Kim & Sanders 1998; Cowie et al. 2004).

The total completeness corrected mass of the SDSS post-starburst galaxies with $\log(\mathrm{M}/\mathrm{M}_{\odot}) > 9.75$ is $6.9^{+1.4}_{-1.3} \times 10^{10} M_{\odot}$, giving a mass density of $1.2 \pm 0.2 \times 10^{4} M_{\odot}/\mathrm{Mpc}^{3}$. This is just 0.43% of the mass density of post-starbursts at $z \sim 0.7$.

As in Section 5.3 an upper limit on the time the post-starbursts are visible for is 0.6 Gyr. Following Equation 3 we find a mass flux of $\dot{\rho}_{A\rightarrow Q,PSB} > 2.0 \pm 0.4 \times 10^{-5}$ $\mathrm{M}_{\odot}/\mathrm{Mpc}^{3}$/yr. Assuming our best estimate for the visibility of the post-starburst galaxies of 0.35 Gyr results in a mass flux of $\dot{\rho}_{A\rightarrow Q,PSB} = 3.4 \pm 0.6 \times 10^{-5}$ $\mathrm{M}_{\odot}/\mathrm{Mpc}^{3}$/yr.

The SED fitting results indicate that two of the low-redshift post-starburst galaxies have no residual star formation (SSFR$<10^{-11}$/yr), while one has a SSFR of 10^{-10}/yr. However, we caution that with only the optical and NIR bands, these values are less reliable than for the VVDS galaxies with UV-IR coverage. We have therefore used all three galaxies to calculate the present day mass flux through the post-starburst phase. The masses of the three SDSS post-starburst galaxies are $\log(\mathrm{M}/\mathrm{M}_{\odot})$=10.25, 10.15 and 10.05, similar to the masses of the VVDS post-starburst galaxies.

We can compare our low redshift PSB mass flux to that calculated by (Martin et al. 2007) for galaxies in the green valley. They assumed that green valley galaxies defined in NUV-r colours in an SDSS/GALEX matched catalogue are all entering the red sequence (i.e. all the mass flows from blue-to-red) to calculate a transition mass flux of $\dot{\rho}_{T} = 0.033\mathrm{M}_{\odot}$/Mpc^{3}/yr. Clearly, this value is considerably greater (a factor of 1,000) than our post-starburst mass flux. If the assumption that all green valley galaxies are heading towards the red-sequence is correct, then the post-starburst pathway to the red sequence appears truly unimportant in the present-day Universe. Some of this discrepancy may be reduced by appealing to the differing mass limits of the two samples. For example, Quintero et al. (2004) studied a sample of post-starburst galaxies in the SDSS, using a similar magnitude limit to that of Martin et al. (2007), which includes many lower mass galaxies than in our sample. They measured the “rate density” for post-starburst galaxies in the SDSS, i.e. the number of galaxies which pass through the post-starburst phase, to be $\sim 4 \times 10^{-5}$/Mpc^{3}/Gyr. The equivalent value for our high-mass sample is $\sim 1.5 \times 10^{-6}$/Mpc^{3}/Gyr strongly suggesting that the measured post-starburst mass flux would increase were we to relax our mass limit.

7 DISCUSSION: ARE POST-STARBURST GALAXIES IMPORTANT?

In this paper we have presented a sample of galaxies with strong Balmer absorption lines and, through comparison with simulations, have argued that these are the likely descendants of gas-rich major mergers. The strength of their spectral features suggest that they are post-starburst galaxies with burst mass fractions of at least 5-10%. However, irrespective of whether a starburst has occurred, it is certain that their star-formation has been quenched quickly with a timescale of $\lesssim$0.1–0.2 Gyr. As discussed briefly in Section 1, such fast quenching times are generally associated with supernovae feedback after periods of rapid star formation induced by galaxy collisions. An alternative scenario may be rapid fueling of star formation in galaxies from filamentary cold-gas flows (Kereš et al. 2005; Ocvirk et al. 2008), although direct comparisons with the outputs of these simulations would be required to test this.

7.1 QSOs and post-starburst galaxies

One popular theory for the origin of the red sequence and the relation between galaxy bulge mass and central supermassive black hole mass is through the triggering of massive outflows driven by the central black hole. Such outflows would quickly halt star formation and therefore the theory suggests an evolutionary link between QSOs and post-starburst galaxies. It is therefore of interest to compare the number density of the post-starburst galaxies to that of QSOs at the same redshift. Any meaningful comparison requires knowledge of the QSO lifetime and the visibility time of the post-starburst galaxies. The former has been estimated using a variety of methods to be $t_{\rm QSO} \sim 10^7$ (see e.g. Gonçalves et al. 2008) and we assume $t_{\rm PSB} = 0.35$ Gyr as previously. Setting

$$\frac{\phi_{\rm QSO}(M < M_X)}{t_{\rm QSO}} = \frac{\phi_{\rm PSB}}{t_{\rm PSB}} \tag{4}$$

we can estimate the magnitude limit of the QSOs, M_X, which leads to a space density matching the observed space density of post-starburst galaxies of 1×10^{-4}/Mpc^3. Using the parameterised QSO luminosity function of Croom et al. (2004) at $z = 0.7$, we find $M_X \approx M^*(z = 0.7) + 1.5 = -22.2$ where the magnitudes are b_j–band and Vega zero-point. That the number density of strong post-starburst galaxies coincides with that of moderately powerful QSOs, 1.5 magnitudes fainter than M^*, does not of course necessarily imply an evolutionary link. The AGN luminosity function continues to rise to fainter magnitudes (Hao et al. 2005) and uncovering the triggering mechanisms of AGN as a function of luminosity remains one of the biggest observational challenges for extragalactic astronomy.

The number density of the post-starburst galaxies evolves rapidly. Extrapolating the evolution of the QSO luminosity function of Croom et al. (2004) to $z = 0.07$, and taking $t_{\rm QSO} \sim 10^7$ as before, we find a QSO number density of 3.1×10^{-5}Mpc^{-3} above the same magnitude limit of $M_X = -22.2$, a factor of a few below the $z = 0.7$ number density. So current results suggest that the evolution in number density of QSOs is not as strong as the evolution in the PSB number density. To our knowledge, an observed QSO luminosity function at $z \sim 0$ is not currently available, and would be required for a more detailed comparison.

7.2 Major mergers and post-starburst galaxies

If, as we have suggested, the strong post-starburst galaxies selected in this paper are the result of major mergers, it is instructive to compare the number of post-starburst galaxies to the number of close galaxy pairs in the same survey volume. de Ravel et al. (2008) measure the fraction of close spectroscopic pairs to derive the merger rate using the same VVDS galaxy sample as in this paper. For galaxies with $\log(\rm M/M_\odot) > 10$ they derive a merger rate of 2×10^{-4}Mpc^{-3}Gyr^{-1}, with a magnitude difference criteria such that they are sensitive to mergers with mass ratios $\gtrsim$4:1. This can be compared with the number of post-starburst galaxies, divided by the time during which they are detectable i.e. 2.9×10^{-4}Mpc^{-3}Gyr^{-1} for $t_{\rm PSB}$ =0.35 Gyr. Given the small number statistics of both samples, uncertainty in both merger and PSB timescales and the problem of the unknown magnitude difference between the PSB progenitors, it is encouraging that these numbers are so close. Of course, larger samples and further detailed observations of the post-starburst galaxies will greatly aid our understanding of their origin and possible link to gas-rich major mergers. As with the QSO number density, the current estimates of the evolution in merger rate with redshift show less evolution than observed in the PSB number density. Although de Ravel et al. (2008) find that the evolution with redshift is stronger for lower luminosity and lower mass galaxies, with the merger rate decreasing by a factor of two between a redshift of 1 and 0.5, this is still not as strong as the evolution in PSB number density. Finally, we note that out of the 36 close galaxy pairs identified by de Ravel et al. (2008) one galaxy is part of the post-starburst sample of this paper. Given the small probability of a chance coincidence, this suggests that in at least one case the post-starburst stellar population is linked with tidal disruption caused by an ongoing major merger.

The strong evolution in PSB number (and mass) density compared to the evolution of both QSO number density and galaxy major merger rate, leads us to the question of what may cause such a sharp decline in the number of post-starburst galaxies. Through our comparison with merger simulations, we have identified two important factors in creating a post-starburst galaxy: gas mass fraction and timescale of the starburst. Larger gas mass fractions provide more fuel for the starburst, leading to stronger and more prolonged post-starburst signatures. Because gas is used-up in the formation of stars, it is reasonable to assume that gas mass fraction decreases with decreasing redshift, a fact that may play a leading role in the global decrease of star formation rate density since $z \sim 1$. A second effect is the starburst timescale, which is generally assumed to be linked to the disk dynamical timescale, which in turn is linked to the dynamical time of the halo. This latter value is known to increase with redshift, by a factor of 2 between a redshift of 1 and 0 (E. Neistein priv. comm., Barkana & Loeb 2001). A lengthening of the duration of the starbursts, together with a decreasing amount of fuel available, may be the dominant mechanism responsible for the decrease in number density of post-starburst galaxies. Clearly further simulations will be required to test these ideas.

7.3 The environments of PSB galaxies

Given the possible link of PSB galaxies to gas-rich major mergers, it is interesting to investigate the local environments of the galaxies. Cucciati et al. (2006) measured the density on 5 and $8h^{-1}$Mpc scales around galaxies in the VVDS survey. Of the 16 PSB galaxies with $\log(\rm M/M_\odot) > 9.75$, 15 have available density measures. A control sample of 2122 VVDS galaxies with good quality redshift flags was selected for comparison. We do not detect any significant difference in the mean or median densities around the PSB galaxies, in agreement with the results of Yan et al. (2008). It is, however, interesting to see that the spread in local density values for the PSB sample is very large. In detail, 3 lie in underdense environments ($\delta_5 < 0$), 9 in normally overdense environments ($0 < \delta_5 < 1$, while the median value for the control sample is $\delta_5 = 0.44 \pm 0.02$) and 3 in strongly overdense environments ($\delta_5 > 1$). Furthermore, there is no clear trend between star-forming vs. non-star-forming PSB galaxies. The presence of PSB galaxies in all types of environment will be an important constraint for understanding their origin and evolution.

7.4 Building the red sequence through post-starburst galaxies

In Section 5.3 we compared the mass flux through the post-starburst phase to the mass build–up of the red sequence as measured by Arnouts et al. (2007). We found a value of ~40% for PSBs with no residual star formation, or 80% for all PSBs with $\log(\mathrm{M}/\mathrm{M}_\odot) > 9.75$. These numbers, although consistent (i.e. not greater than 100%), perhaps still appear surprisingly high if we expect other quenching mechanisms with slower timescales to also play a role in moving mass onto the red sequence (van den Bosch et al. 2008). The key question is whether there is a one–way flow of galaxies from the blue to the red sequence? What prevents a galaxy from re-starting star formation due to subsequent inflow of gas after experiencing a major merger? SPH simulations of galaxy mergers invoke strong mechanical AGN feedback to prevent subsequent star formation and allow the galaxy to remain on the red-sequence. The large amount of mass flowing to the red sequence through the post-starburst phase at high redshift, may in fact cause us to question the fact that strong mechanical feedback is effective in the long-term for the majority of galaxies. Semi-analytic cosmological models provide one method to test galaxy formation scenarios in a full cosmological context and could help to understand the directions of mass fluxes. A full comparison of the recent star formation histories of the VVDS and SDSS galaxies presented in this paper with semi-analytic models is underway. A full census of different types of transition galaxies as a function of redshift, when combined with accurate measurements of the mass densities on the blue and red sequence, will help to reveal the true importance of mechanical gas expulsion mechanisms (feedback) on the global evolution of the galaxy population.

We have found that strong post-starburst galaxies have stellar masses similar to those of the least massive galaxies on the red sequence. This has important implications for our understanding of the physical processes involved in the build-up of the red sequence, and in particular the subsequent role of dry-mergers in forming the shape of the red sequence mass function observed today (Bell et al. 2006; Naab et al. 2006).

8 SUMMARY

Using a PCA analysis of the spectra of the VVDS deep spectroscopic galaxy survey, we have selected a sample of 16 galaxies with strong Balmer absorption lines at $0.5 < z < 1.0$ and above a mass completeness limit of $\log(\mathrm{M}/\mathrm{M}_\odot) > 9.75$. Through comparison with a suite of SPH merger simulations and toy starburst models we have shown that these galaxies are likely to have undergone a strong starburst within the last few tenths of a Gyr, with burst mass fractions of order 10%, similar to those derived for LIRGS at these redshifts (Marcillac et al. 2006). The key requirement for the observation of the post-starburst galaxies, is a fast quenching timescale of $\lesssim 0.1 - 0.2$ Gyr. We show that there is a maximum visible lifetime for the post-starburst galaxies of 0.6 Gyr, but for lower gas mass fractions of ~20-40% a lifetime of 0.35 Gyr is more likely.

The key results of this paper are:

- **Number density:** PSB galaxies with $\log(\mathrm{M}/\mathrm{M}_\odot) > 9.75$ have a number density of 10^{-4} per Mpc^3. Assuming they are visible for an average of 0.35 Gyr, and that a QSO shines for 10^7 years, this is equal to the number density of QSOs brighter than $M^*(z = 0.7) + 1.5$ (Croom et al. 2004).
- **Masses and mass density:** Summing all the mass in the post-starburst population gives a mass density of $\log(\rho^*/\mathrm{M}_\odot/\mathrm{Mpc}^3) = 6.43^{+0.06}_{-0.04}$. The mass distribution of the PSB galaxies rises to the mass completeness limit of $\log(\mathrm{M}/\mathrm{M}_\odot) > 9.75$, therefore measuring the complete mass distribution for post-starburst galaxies at $z \sim 0.7$ will require a deeper survey. The true mass distribution is crucial for understanding the relative importance of different mechanisms for causing post-starburst galaxies (Kaviraj et al. 2007).
- **Mass flux:** We select the 5 PSB galaxies with no residual star formation according to multiwavelength SED fitting. Taking 0.6 Gyr as an upper limit on the visibility time of the PSB galaxies gives a lower limit on the mass flux of $\dot{\rho}_{A \rightarrow Q,PSB} > 0.0022^{+0.0002}_{-0.006}$ M$_\odot$/Mpc^3/yr. Taking our best estimate for t_{PSB} of 0.35 Gyr gives $\dot{\rho}_{A \rightarrow Q,PSB} = 0.0038^{+0.0004}_{-0.001}$ M$_\odot$/Mpc^3/yr. Comparing this to the rate of build up of the red sequence (Arnouts et al. 2007), we find 38^{+4}_{-11}% of the growth of the red sequence at $z < 1$ takes place from galaxies which have passed through the strong post-starburst phase, assuming all these galaxies subsequently remain on the red sequence.
- **Environment:** We use the local density on $5h^{-1}$Mpc scales from Cucciati et al. (2006) to show that PSB galaxies are found in all environments, from underdense to strongly overdense.
- **Low vs. High z:** We compare our high-redshift results to a sample of galaxies with $0.05 < z < 0.1$ selected from the SDSS and UKIDSS surveys. Despite the enormous increase in sample size, only 3 post-starburst galaxies of the same strength as in the VVDS sample are detected for the same mass limit. We find the mass density of strong post-starburst galaxies decreases by a factor of 230 and number density by a factor of 200 from $z \sim 0.7$ to $z \sim 0.07$ (see also Hammer et al. 1997; Le Borgne et al. 2006).

This paper finds that post-starburst galaxies, although rare in the local Universe, are of global importance at higher redshift. With larger and deeper spectroscopic surveys, exciting new constraints could be obtained on the processes which drive galaxy evolution. The joint analysis of imaging and spectroscopy will help to break observational degeneracies, especially when combined with "observations" of galaxy simulations. On the advent of an era of large broad band photometric surveys, it is important not to forget the wealth of additional information on galaxy evolution available from the additional investment in spectroscopy.

ACKNOWLEDGMENTS

The authors would like to thank Celine Eminian and Steve Warren for their help with using the UKIDSS survey; Henry McCracken for all his help with the VVDS and CFHTLS surveys and the photo-zs, and Olivier Ilbert for aiding our understanding of the photometric catalog generation; Olga Cucciati for providing the density measurements for the VVDS galaxies; Christy Tremonti, Crystal Martin, John Silverman and Eyal Neistein for interesting discussions; the MAGPop Network and especially PI Guinevere Kauffmann for providing the networking opportunity that led to the start of this project; and the anonymous referee for their careful reading of the manuscript and constructive comments for improvement. VW acknowledges an Institut d'Astrophysique EARA visitor grant and the Aspen center for Physics for providing the quiet surroundings in which this paper was mostly written. During this project, VW and CJW were supported by the EU MAGPop Marie Curie network. AP was financed by the research grant of the Polish Ministry of Science PBZ/MNiSW/07/2006/34A.

The numerical simulations were performed on the Munich Observatory SGI-Altix 3700 Bx2 machine, which was partly funded by the Cluster of Excellence: "Origin and Structure of the Universe"

References

Adelman-McCarthy J. K., et al. 2007, ApJS, 172, 634
Arnouts S., Walcher C. J., Le Fèvre O., et al. 2007, A&A, 476, 137
Baldry I. K., Glazebrook K., Brinkmann J., Ivezić Ž., Lupton R. H., Nichol R. C., Szalay A. S., 2004, ApJ, 600, 681
Balogh M. L., Morris S. L., 2000, MNRAS, 318, 703
Barger A. J., Cowie L. L., Mushotzky R. F., Yang Y., Wang W.-H., Steffen A. T., Capak P., 2005, AJ, 129, 578
Barkana R., Loeb A., 2001, Physics Reports, 349, 125
Barnes J. E., Hernquist L., 1992, ARAA, 30, 705
Bell E. F., Naab T., McIntosh D. H., et al. 2006, ApJ, 640, 241
Bell E. F., Wolf C., Meisenheimer K., et al., 2004, ApJ, 608, 752
Binette L., Magris C. G., Stasińska G., Bruzual A. G., 1994, A&A, 292, 13
Böker T., Sarzi M., McLaughlin D. E., van der Marel R. P., Rix H.-W., Ho L. C., Shields J. C., 2004, AJ, 127, 105
Bondi H., Hoyle F., 1944, MNRAS, 104, 273
Brinchmann J., Charlot S., White S. D. M., Tremonti C., Kauffmann G., Heckman T., Brinkmann J., 2004, MNRAS, 351, 1151
Bruzual G., Charlot S., 2003, MNRAS, 344, 1000
Budavari T., Wild V., Szalay A. S., Dobos L., Yip C.-W., 2008, ArXiv e-prints 0809.0881, MNRAS accepted
Bundy K., Ellis R. S., Conselice C. J., 2005, ApJ, 625, 621
Bundy K., Ellis R. S., Conselice C. J., et al., 2006, ApJ, 651, 120
Casali M., Adamson A., Alves de Oliveira C., et al. 2007, A&A, 467, 777
Cayatte V., Kotanyi C., Balkowski C., van Gorkom J. H., 1994, AJ, 107, 1003
Chabrier G., 2003, PASP, 115, 763
Chapman S. C., Blain A. W., Smail I., Ivison R. J., 2005, ApJ, 622, 772
Charlot S., Fall S. M., 2000, ApJ, 539, 718
Cid Fernandes R., Mateus A., Sodré L., Stasińska G., Gomes J. M., 2005, MNRAS, 358, 363
Connolly A. J., Szalay A. S., 1999, AJ, 117, 2052
Cowie L. L., Barger A. J., Fomalont E. B., Capak P., 2004, ApJL, 603, L69
Cox T. J., Jonsson P., Somerville R. S., Primack J. R., Dekel A., 2008, MNRAS, 384, 386
Croom S. M., Smith R. J., Boyle B. J., Shanks T., Miller L., Outram P. J., Loaring N. S., 2004, MNRAS, 349, 1397
Cucciati O., Iovino A., Marinoni C., et al. 2006, A&A, 458, 39
da Cunha E., Charlot S., Elbaz D., 2008, MNRAS, 388, 1595
de Ravel L., Le Fèvre O., Tresse L., et al. 2008, ArXiv e-prints, 0807.2578
Faber S. M., Willmer C. N. A., Wolf C., et al. 2007, ApJ, 665, 265
Franzetti P., Scodeggio M., Garilli B., et al. 2007, A&A, 465, 711
Gonçalves T. S., Steidel C. C., Pettini M., 2008, ApJ, 676, 816
Gunn J. E., Gott J. R. I., 1972, ApJ, 176, 1
Hambly N. C., Collins R. S., Cross N. J. G., et al. 2008, MNRAS, 384, 637
Hammer F., Flores H., Lilly S. J., et al., 1997, ApJ, 481, 49
Hao L., Strauss M. A., Fan X., et al. 2005, AJ, 129, 1795
Hernquist L., 1990, ApJ, 356, 359
Hewett P. C., Warren S. J., Leggett S. K., Hodgkin S. T., 2006, MNRAS, 367, 454
Hopkins P. F., Bundy K., Hernquist L., Ellis R. S., 2007, ApJ, 659, 976
Hubble E. P., 1926, ApJ, 64, 321
Ilbert O., Arnouts S., McCracken H. J., et al. 2006, A&A, 457, 841
Ilbert O., Tresse L., Arnouts S., et al. 2004, MNRAS, 351, 541
Ilbert O., Tresse L., Zucca E., et al. 2005, A&A, 439, 863
Iovino A., McCracken H. J., Garilli B., et al. 2005, A&A, 442, 423
Johansson P. H., Naab T., Burkert A., 2009, ApJ, 690, 802
Kauffmann G., Heckman T. M., White S. D. M., et al., 2003a, MNRAS, 341, 33
Kauffmann G., Heckman T. M., White S. D. M., et al., 2003b, MNRAS, 341, 54
Kaviraj S., Kirkby L. A., Silk J., Sarzi M., 2007, MNRAS, 382, 960
Kereš D., Katz N., Weinberg D. H., Davé R., 2005, MNRAS, 363, 2
Khalatyan A., Cattaneo A., Schramm M., Gottlöber S., Steinmetz M., Wisotzki L., 2008, MNRAS, 387, 13
Khochfar S., Burkert A., 2006, A&A, 445, 403
Kim D.-C., Sanders D. B., 1998, ApJS, 119, 41
Koleva M., Prugniel P., Ocvirk P., Le Borgne D., Soubiran C., 2008, MNRAS, 385, 1998
Larson R. B., Tinsley B. M., Caldwell C. N., 1980, ApJ, 237, 692
Lawrence A., Warren S. J., Almaini O., et al. 2007, MNRAS, 379, 1599
Le Borgne D., Abraham R., Daniel K., et al., 2006, ApJ, 642, 48
Le Fèvre O., Mellier Y., McCracken H. J., et al. 2004, A&A, 417, 839
Le Fèvre O., Vettolani G., Garilli B., et al. 2005, A&A, 439, 845
Lonsdale C. J., Smith H. E., Rowan-Robinson M., et al. 2003, PASP, 115, 897
Lotz J. M., Jonsson P., Cox T. J., Primack J. R., 2008, MNRAS, 391, 1137
Marcillac D., Elbaz D., Charlot S., Liang Y. C., Hammer F., Flores H., Cesarsky C., Pasquali A., 2006, A&A, 458, 369
Martin D. C., Fanson J., Schiminovich D., et al. 2005, ApJL, 619, L1
Martin D. C., Wyder T. K., Schiminovich D., et al. 2007, ApJS, 173, 342
McCracken H. J., Radovich M., Bertin E., et al. 2003, A&A, 410, 17
Naab T., Burkert A., 2003, ApJ, 597, 893
Naab T., Johansson P. H., Ostriker J. P., Efstathiou G., 2007, ApJ, 658, 710
Naab T., Khochfar S., Burkert A., 2006, ApJL, 636, L81
Noeske K. G., Weiner B. J., Faber S. M., et al. 2007, ApJL, 660, L43

Ocvirk P., Pichon C., Teyssier R., 2008, MNRAS, 390, 1326
Osterbrock D. E., 1989, Astrophysics of gaseous nebulae and active galactic nuclei. University Science Books, Mill Valley, CA
Panter B., Heavens A. F., Jimenez R., 2003, MNRAS, 343, 1145
Pozzetti L., Bolzonella M., Lamareille F., et al. 2007, A&A, 474, 443
Quintero A. D., Hogg D. W., Blanton M. R., et al. 2004, ApJ, 602, 190
Salim S., Charlot S., Rich R. M., et al. 2005, ApJL, 619, L39
Schawinski K., Thomas D., Sarzi M., Maraston C., Kaviraj S., Joo S.-J., Yi S. K., Silk J., 2007, MNRAS, 382, 1415
Schmidt M., 1968, ApJ, 151, 393
Springel V., 2005, MNRAS, 364, 1105
Springel V., Di Matteo T., Hernquist L., 2005a, ApJL, 620, L79
Springel V., Di Matteo T., Hernquist L., 2005b, MNRAS, 361, 776
Springel V., Hernquist L., 2003, MNRAS, 339, 289
Storey P. J., Hummer D. G., 1995, MNRAS, 272, 41
Strateva I., Ivezić Ž., Knapp G. R., et al. 2001, AJ, 122, 1861
Strauss M. A., Weinberg D. H., et al. (The SDSS Collaboration), 2002, AJ, 124, 1810
Tojeiro R., Heavens A. F., Jimenez R., Panter B., 2007, MNRAS, 381, 1252
Toomre A., Toomre J., 1972, ApJ, 178, 623
Tran K.-V. H., Franx M., Illingworth G. D., van Dokkum P., Kelson D. D., Magee D., 2004, ApJ, 609, 683
Tresse L., Ilbert O., Zucca E., et al. 2007, A&A, 472, 403
van den Bosch F. C., Aquino D., Yang X., Mo H. J., Pasquali A., McIntosh D. H., Weinmann S. M., Kang X., 2008, MNRAS, 387, 79
van Dokkum P. G., 2005, AJ, 130, 2647
Vergani D., Scodeggio M., Pozzetti L., et al. 2008, A&A, 487, 89
Walcher C. J., Lamareille F., Vergani D., et al. 2008, A&A, 491, 713
Wild V., Kauffmann G., Heckman T., Charlot S., Lemson G., Brinchmann J., Reichard T., Pasquali A., 2007, MNRAS, 381, 543
Willmer C. N. A., Faber S. M., Koo D. C., et al. 2006, ApJ, 647, 853
Yan R., Newman J. A., Faber S. M., et al. 2008, ArXiv e-prints 0805.0004
Yan R., Newman J. A., Faber S. M., Konidaris N., Koo D., Davis M., 2006, ApJ, 648, 281